THESIS FOR THE DEGREE OF LICENTIATE OF ENGINEERING

Pd-nanoalloys for hydrogen sensing: Multiscale modeling of thermodynamic and optical properties

Pernilla Ekborg-Tanner

Department of Physics
CHALMERS UNIVERSITY OF TECHNOLOGY
Göteborg, Sweden 2022

Pd-nanoalloys for hydrogen sensing: Multiscale modeling of thermodynamic and optical properties
Pernilla Ekborg-Tanner

Department of Physics
Chalmers University of Technology
se-412 96 Göteborg, Sweden
Telephone +46 (0)31 772 10 00

Cover: Illustration of a Pd nanodisk in a hydrogen environment.

Chalmers digitaltryck
Göteborg, Sweden 2022

Pd-nanoalloys for hydrogen sensing: Multiscale modeling of thermodynamic and optical properties

Pernilla Ekborg-Tanner
Department of Physics
Chalmers University of Technology

Abstract

Hydrogen sensing based on Pd nanoalloys has shown great promise in the past decades and could potentially be part of a solution that enables a safe future hydrogen economy. There are, however, remaining challenges related to, e.g., long-term stability and therefore a need for further optimization of these systems. Computational methods provide means to efficiently explore possible combinations of alloyants, composition, and nanostructure geometry. This thesis focuses on two aspects of sensor optimization: surface segregation and hydrogen sensitivity, using multi-scale modeling approaches.

Alloying Pd with metals such as Au and Cu is necessary to overcome issues related to hysteresis and CO poisoning. At the same time, it introduces additional difficulties related to the chemical order such as surface segregation, which is directly related to long-term stability. In this thesis, the surface composition of Pd alloyed with Au or Cu is studied as a function of H_2 pressure using Monte Carlo simulations based on cluster expansions parametrized against ab-initio calculations. For Pd–Au, an increased H_2 concentration abruptly switches the surface from Au to Pd dominant. For Pd–Cu, the change with H_2 concentration is much more gradual with non-monotonic tendencies, with an overall surplus of Pd in most conditions.

The sensing principle is based on the shift in optical response upon H absorption. The magnitude of the sensor readout at a certain H_2 pressure depends on nanoparticle geometry and alloy composition. In this thesis, extinction spectra are calculated for Pd–Au–H nanodisks using electrodynamic simulations and the corresponding H sensitivity is analyzed. It is found that the H sensitivity depends on the nanodisk diameter, mainly due to the interplay between a localized surface plasmon and an interband transition which becomes more apparent for smaller nanodisks.

Keywords: hydrogen sensing, Pd-alloys, surface segregation, nanoalloys, nanoplasmonics

LIST OF APPENDED PAPERS

This thesis is partly based on work presented in the following papers:

I **Hydrogen-driven Surface Segregation in Pd-alloys from Atomic Scale Simulations**
Pernilla Ekborg-Tanner and Paul Erhart
The Journal of Physical Chemistry C **125**, 17248–17260 (2021)

II **Computational Design of Alloy Nanostructures for Optical Sensing: The Limits of Tuning Hydrogen Sensitivity via Composition and Geometry**
Pernilla Ekborg-Tanner, J. Magnus Rahm, Victor Rosendal, Tuomas P. Rossi, Tomasz J. Antosiewicz, and Paul Erhart
In manuscript

The author's contribution to the papers:

I I carried out the majority of the calculations and simulations, analyzed the results and wrote the paper with assistance from my co-author.

II I carried out the FDTD simulations, analyzed the corresponding results and wrote the majority of the paper with assistance from my co-authors.

Contents

List of abbreviations

ARDR automatic relevance detection regression. 12

CE cluster expansion. 10–16, 24, 37, 41, 42

DF dielectric function. 3, 17, 19, 29–35, 38

DFT density-functional theory. 5, 6, 9, 13, 25, 27, 37, 42

ECI effective cluster interaction. 11, 12, 41

fcc face-centered cubic. 12, 24, 25, 27, 37, 41

FDTD finite-difference time-domain. 17–19, 31, 38, 42

GGA generalized-gradient approximation. 9, 10

KS Kohn-Sham. 6–8

LASSO least absolute shrinkage and selection operator. 12

LDA local density approximation. 9, 10

LSPR localized surface plasmon resonance. 2, 3, 29–35, 38, 39

MC Monte Carlo. 14–16, 37

NN nearest neighbor. 12

NP nanoparticle. 2, 3, 16, 24, 29, 30, 41

OLS ordinary least-squares. 12

PAW projected augmented wave. 9

PBC periodic boundary condition. 8

PML perfectly matched layer. 18

RFE recursive feature elimination. 12

RPA random phase approximation. 42

SGC semi-grand canonical. 15, 16

TDDFT time-dependent density-functional theory. 38

vdW-DF van der Waals density functionals. 9

XC exchange-correlation. 7, 9, 42

1 Introduction

The hydrogen economy is a proposed future energy system where hydrogen (H) is the primary energy carrier. Hydrogen gas (H_2) has the highest known gravimetric energy density and can be produced from naturally abundant, green sources [1] which makes it an appealing replacement for fossil fuels. Hydrogen-driven devices typically operate via fuel cells and exist in a range of scales; from ~1 W portable units to ~1 MW stationary electric power plants [2]. Recently, fuel cells have gained attention in the field of heavy vehicles (~100 kW) such as trucks [3], buses [4] and trains [5], in particular, where other green technologies such as battery electric vehicles might be less attractive due to issues with weight and material abundance. The large scale implementation of a hydrogen economy is, however, still hindered by remaining issues related to production [1, 6], storage [1, 7], and safety [8].

This thesis is related to the safety aspect which stems from the flammability of H_2 mixed in air. Since leaks can never be completely avoided, efficient hydrogen sensing is a necessity in order to ensure safe storage and usage of H_2. Hydrogen sensing is an active field and several different techniques have been proposed, generally based on the change in optical [9–21] or electrical [22–24] properties of a material during H absorption. The electronic properties of a material before and after H absorption differ, which can lead to a shift in, e.g., the optical response or resistivity. The principle of a hydrogen sensor is to detect such a change and relate it to the H_2 pressure in the surroundings.

In this work, the focus is on plasmonic hydrogen sensors based on nanostructures consisting of palladium based alloys (Pd-nanoalloys). The combination of nanoengineering and alloying results in a practically endless number of nanoalloys imaginable, by means of varying the geometry, alloyants, and composition(s). Computational modeling enables efficient exploration of a large set of systems since the time and cost associated with experimental studies is greatly reduced. The objective of this thesis is to develop such approaches and apply them to issues related to function optimization, fab-

rication conditions, and long term stability of Pd-based hydrogen sensors. In particular, the aim is to answer the following questions:

- What is the surface segregation behavior of Pd-alloys in different environments?
- How does the composition and geometry affect the optical response?

To this end, multiscale modeling techniques are employed starting from the electronic properties at the nanoscale via thermodynamic averages of thousands of atoms to the continuum optical properties at the mesoscopic scale.

1.1 Pd-based nanoplasmonic hydrogen sensing

If a Pd nanoparticle (NP) is placed in a light source, which causes an electromagnetic field, its electrons can begin to oscillate collectively, i.e., moving from one side of the NP to the other in a synchronized fashion. This phenomenon is called localized surface plasmon resonance (LSPR), where a plasmon is the collective oscillation of electrons and "localized" refers to the fact the plasmon is confined to the small space spanned by the NP (as opposed to a bulk plasmon in a large-scale material). The excitation of a plasmon leads to an increase in optical extinction at the resonance frequency corresponding to the oscillation and appears as a peak in a measured extinction spectrum. As the Pd NP absorbs H, the electronic properties change and accordingly, the plasmon peak shifts to a slightly different, in general smaller, frequency.

Pd-based materials are furthermore often referred to as hydrogen sponges due to their excellent ability to quickly absorb and desorb H. This fact, together with the plasmon peak shift upon H absorption, is the basis of Pd-based nanoplasmonic hydrogen sensing. The H content of the NP, and in extension its optical response, quickly adjusts to the instantaneous H_2 pressure. By measuring, e.g., the peak position as a function of time and calibrating it against the H_2 pressure, a hydrogen sensor is obtained. Such a hydrogen sensor was first suggested by Langhammer *et al.* in 2007 [11] and has been a subject of research ever since [12, 18, 25–27].

1.2 Alloying to improve material properties

Alloying is a common strategy for introducing tunability in materials engineering that has also been successful in the case of Pd-based nanoplasmonic hydrogen sensing. A major issue with Pd NPs is the fact that H absorption in Pd is associated with phase separation, which causes hysteresis in the measured H_2 pressure vs absorption isotherms during uptake and release. As a consequence, the sensor cannot accurately give information on the surrounding pressure in this region. The hysteresis can, however, be removed by alloying with gold (Au) [15, 27, 28].

In addition, Pd NPs are subject to CO poisoning, i.e., the deactivation of hydrogen sensors caused by CO molecules binding to the surface, which effectively blocks hydrogen adsorption. Alloying with copper (Cu) has been found to inhibit this effect in experimental studies [29]. It is crucial to avoid both hysteresis and CO poisoning in order to achieve reliable and long-term stable hydrogen sensors. Fortunately, recent studies show that by alloying with 25% Au and 10% Cu, both of these issues can be addressed simultaneously [29, 30].

At the same time, alloying increases the complexity of the system, which makes the materials properties harder to predict. Most notably, the chemical ordering of the atoms has to be considered which gives rise to phenomena such as ordering, phase separation, and surface segregation. The surface state of a hydrogen sensor is crucial for its functionality since H absorption takes place via the surface and the associated energy barriers depend on the atomic species in the surface region. Understanding the surface segregation is thus important. To further complicate the situation, surface segregation depends on the environment. As a result, there will generally be a huge difference between a sensor fabricated in vacuum conditions vs. in H_2 and the long term stability is affected by the conditions during storage and operation.

1.3 Structure of thesis

The remainder of this thesis is structured as follows. In Chapter 2, the computational methods used in this thesis are presented and their background theory briefly covered. Then follow two chapters on the most important topics of this thesis: the thermodynamic and optical properties of hydrogenated Pd-alloys. First, in Chapter 3, the thermodynamics are covered with emphasis on how the bulk and surface states depend on composition and the presence of hydrogen based on theory, previous studies and the most important findings within this thesis. Second, in Chapter 3, the optical properties are covered including classical theory on LSPR and the dielectric function (DF) as well as how these concepts are related to the optical response of Pd–Au–H nanodisks. In Chapter 5, the two papers that make up the basis of this thesis are summarized. Lastly, in Chapter 6, we return to the main questions of this thesis: what is the surface segregation behavior of Pd-alloys in different environments and how does the composition and geometry affect their optical response? In particular, we reflect on the answers and discuss remaining challenges for future studies.

2 Computational methods

This thesis builds on a range of computational methods covering multiple length scales. In this chapter, these methods are introduced and their background theory briefly presented.

2.1 Density functional theory

In several fields of materials research it is of interest to calculate the quantum mechanical properties of interacting many-body systems. For the large majority of such systems, this is not feasible using exact analytic methods and we have to resort to numerical methods and approximations. A popular choice is density-functional theory (DFT), which can be used to calculate the quantum-mechanical ground state of systems consisting of up to thousands of atoms. In this thesis, the Vienna Ab initio Simulation Package (VASP) [31, 32] is used for all DFT calculations. This section provides a brief presentation of the theoretical framework of DFT, based on Ref. [33].

2.1.1 The Hohenberg-Kohn theorems

Consider a many-body system consisting of electrons and nuclei. Since nuclei are much heavier than electrons, from the perspective of the nuclei the electrons adjust instantaneously to any movement of the nuclei while the nuclei appear frozen in the view of the electrons. Using the Born-Oppenheimer approximation [34], the nuclei can be regarded as fixed when solving for the electron ground state and contributions involving only the nuclei are typically treated classically.

The Hamiltonian for the electrons of a many-body system with fixed nuclei can be written in Hartree atomic units ($\hbar = m_e = e = 4\pi\epsilon_0 = 1$) as [33, Chapter 6]

$$\hat{H} = -\frac{1}{2}\sum_i \nabla_i^2 + \sum_i V_{\text{ext}}(\boldsymbol{r}_i) + \frac{1}{2}\sum_{i\neq j}\frac{1}{|\boldsymbol{r}_i - \boldsymbol{r}_j|}, \tag{2.1}$$

where the first term is the kinetic energy, the second is due to an external potential $V_{\text{ext}}(\boldsymbol{r})$ (including the interaction between electrons and fixed nuclei) and the last is the Coulomb interaction between electrons. For most systems, it is not feasible to solve the corresponding Schrödinger equation, but the problem can be simplified using DFT.

The basis of DFT are two theorems first proved by Hohenberg and Kohn in 1964 [35]. The first theorem states that the external potential $V_{\text{ext}}(\boldsymbol{r})$, and in turn all properties of the many-body system, are determined by the ground state electron density $n_0(\boldsymbol{r})$. The second theorem states that a total energy functional $E[n]$ of the electron density $n(\boldsymbol{r})$ can be defined, valid for any $V_{\text{ext}}(\boldsymbol{r})$, and the density that minimizes this functional is the exact ground state electron density $n_0(\boldsymbol{r})$. As a result of these theorems, it is, in principle, enough to find and minimize the functional $E[n]$ to obtain all properties of the system. Multiple issues still remain, however, such as how to find the total energy functional and how to solve the many-body problem (which is, in principle, made possible by the determination of $V_{\text{ext}}(\boldsymbol{r})$) which would yield the wavefunctions and in turn, all properties. The issue of finding the energy functional will be tackled in the remainder of this section, which will result in a feasible approach to find the ground state energy.

2.1.2 The Kohn-Sham ansatz

A general expression for the total energy functional of the interacting many-body system is [33, Chapter 6]

$$E_{\text{HK}}[n] = T[n] + E_{\text{int}}[n] + \int \mathrm{d}\boldsymbol{r} V_{\text{ext}}(\boldsymbol{r}) n(\boldsymbol{r}) + E_{II}, \tag{2.2}$$

where T and E_{int} are the kinetic and potential energy contributions of the electrons, respectively, and E_{II} is the ion-ion interaction energy of the nuclei.

To simplify the problem further, the Kohn-Sham (KS) ansatz [36] is used, where the many-body problem is replaced by an auxiliary non-interacting problem of independent electrons. The underlying assumption is that the independent-particle problem can be defined such that both problems share the same ground state density. Although there are no rigorous proofs for this assumption, it will be regarded as valid in the following. The total energy functional Eq. 2.2 of the interacting many-body problem can be rewritten in terms of the non-interacting problem as [33, Chapter 7]

$$E_{\text{KS}}[n] = T_{\text{KS}}[n] + E_{\text{Hart}}[n] + E_{\text{xc}}[n] + \int \mathrm{d}\boldsymbol{r} V_{\text{ext}}(\boldsymbol{r}) n(\boldsymbol{r}) + E_{II}, \tag{2.3}$$

where T_{KS} is the independent-particle kinetic energy and $E_{\mathrm{Hart}}[n]$ is the Hartree energy,

$$E_{\mathrm{Hart}}[n] = \frac{1}{2}\int \mathrm{d}\boldsymbol{r}\mathrm{d}\boldsymbol{r}' \frac{n(\boldsymbol{r})n(\boldsymbol{r}')}{|\boldsymbol{r}-\boldsymbol{r}'|},$$

i.e., the Coulomb interaction energy in terms of the electron density. The complex many-body effects are grouped into the exchange-correlation (XC) functional $E_{\mathrm{xc}}[n]$, which physically represents the difference in kinetic and internal energy of the electrons in the non-interacting and interacting systems. The last two terms are exactly the same as in Eq. 2.2. If the XC functional is known, the ground state energy and density of the interacting many-body problem can be found by solving the auxiliary problem.

Solution of the auxiliary problem is equivalent to minimizing E_{KS} (Eq. 2.3) under the constraint of constant number of electrons, which can be done using the Lagrange multiplier method [33, Chapter 7]. This procedure leads to the Schrödinger-like KS equations (Eq. 2.4-2.6)

$$\left(\hat{H}_{\mathrm{KS}} - \epsilon_i\right)\psi_i(\boldsymbol{r}) = 0, \tag{2.4}$$

where $\hat{H}_{\mathrm{KS}}$ is the effective Hamiltonian

$$\hat{H}_{\mathrm{KS}} = -\frac{1}{2}\nabla^2 + V_{\mathrm{KS}}(\boldsymbol{r}), \tag{2.5}$$

and $V_{\mathrm{KS}}(\boldsymbol{r})$ is the effective KS potential

$$V_{\mathrm{KS}}(\boldsymbol{r}) = V_{\mathrm{ext}}(\boldsymbol{r}) + \frac{\delta E_{\mathrm{Hart}}}{\delta n(\boldsymbol{r})} + \frac{\delta E_{\mathrm{xc}}}{\delta n(\boldsymbol{r})} = V_{\mathrm{ext}}(\boldsymbol{r}) + V_{\mathrm{Hart}}(\boldsymbol{r}) + V_{\mathrm{xc}}(\boldsymbol{r}). \tag{2.6}$$

Here, ϵ_i and $\psi_i(\boldsymbol{r})$ are the eigenvalues and KS wavefunctions of the non-interaction system. The corresponding ground state density for a system of N electrons is

$$n_0(\boldsymbol{r}) = \sum_{i=1}^{N} |\psi_i(\boldsymbol{r})|^2, \tag{2.7}$$

where ψ_i are the N wavefunctions with the lowest eigenvalues ϵ_i.

2.1.3 Solving the Kohn-Sham equations

Solving the KS equations requires knowledge of the effective potential V_{KS} (Eq. 2.6), which is a functional of the density, but the density is only known once the problem is solved. To get around this paradox, a self-consistent approach is used consisting of the following steps [33, Chapter 9]:

1. Set the ground state density to an initial guess.

2. Calculate the effective potential (Eq. 2.6).
3. Solve the KS equation (Eq. 2.4).
4. Calculate the new density (Eq. 2.7).
5. If the new density is consistent with the previous one, the problem is solved. Otherwise, repeat from step 2 with an updated density.

The resulting self-consistent density has to correspond to the ground state density. The ground state energy (as well other properties such as forces and stresses) of the interacting system can thus be calculated via the total energy functional Eq. 2.3.

The ground state density in each iteration is calculated based on a set of KS wave functions. For crystalline materials, which have periodic boundary conditions (PBCs), the wave functions are typically expanded in terms of plane waves restricted to the first Brillouin zone [33, Chapter 12]. For systems without PBCs in all directions, such as surfaces and molecules, plane waves can still be used by introducing periodic systems with a large separation in space in the direction(s) without a PBC. The wave functions reads

$$\psi_{i,\boldsymbol{k}}(\boldsymbol{r}) = \sum_{G} c_{i,G}(\boldsymbol{k})\, e^{i(\boldsymbol{k}+G)\cdot\boldsymbol{r}}, \tag{2.8}$$

where $c_{i,G}(\boldsymbol{k})$ are Fourier coefficients, $\boldsymbol{k}$ is a wave vector and $\boldsymbol{G}$ are reciprocal lattice vectors. The effective KS potential has the periodicity of the lattice and can be expressed as a sum of Fourier components

$$V_{\mathrm{KS}}(\boldsymbol{r}) = \sum_{G} V_{\mathrm{KS}}(\boldsymbol{G}) e^{i\boldsymbol{G}\cdot\boldsymbol{r}}. \tag{2.9}$$

Lastly, the KS equation (Eq. 2.4) can be expressed in $\boldsymbol{k}$-space

$$\sum_{G'} H_{G,G'}(\boldsymbol{k}) c_{i,G'}(\boldsymbol{k}) = \epsilon_i(\boldsymbol{k}) c_{i,G}(\boldsymbol{k}), \tag{2.10}$$

where

$$H_{G,G'}(\boldsymbol{k}) = \frac{1}{2}|\boldsymbol{k}+\boldsymbol{G}|^2 \delta_{G,G'} + V_{\mathrm{KS}}(\boldsymbol{G}-\boldsymbol{G'}). \tag{2.11}$$

This expansion is truncated by an energy cutoff associated with the wave vector $|\boldsymbol{k}+\boldsymbol{G}|$.

A plane wave basis set is suitable for capturing the periodicity of the system, but less suitable for capturing the rapid variations in the wave function close to the atomic cores (in contrast to, e.g., a basis set based on atomic orbitals). As a result, high energy cutoffs are required for accurate descriptions which comes with a high computational cost. To simplify the problem, the concept of pseudopotentials can be used in which an effective potential is created for the joint effect of the nuclei and core electrons acting on the valence electrons [33, Chapter 11]. The pseudopotentials need to be constructed for

each atomic species separately prior to the DFT calculation. By using pseudopotentials, the valence electron wave functions are smooth close to the atomic core and the computational cost can be reduced. A related, more complex approach which is used in this thesis is the projected augmented wave (PAW) method [37, 38], which introduces a linear transformation between the full wave function and the smooth wave functions, allowing for treatment of the valence and core states at different levels. The PAW method is often accompanied with the frozen-core approximation [39], which means that the core electron wave functions are not updated during the self-consistency cycle.

2.1.4 The exchange-correlation functional

A crucial aspect remains, namely determining the XC functional $E_{\text{xc}}[n]$. The equivalence between the total energy functional of the interacting (Eq. 2.2) and non-interacting (Eq. 2.3) systems holds only if the XC is known exactly [33, Chapter 7]. In practice, however, this functional has to be approximated. A large number of XC functionals has been proposed, each with their own strengths and shortcomings, and the choice of functional has to be made with regard to the system under study, the properties of interest, and the available computational resources.

Since the kinetic and long-range Hartree energy contributions have been separated out from the total energy functional, the XC functional can be approximated as a (nearly) local functional of the density [33, Chapter 8]. The simplest approach is the local density approximation (LDA), which reads

$$E_{\text{xc}}^{\text{LDA}}[n] = \int \mathrm{d}\boldsymbol{r}\, n(\boldsymbol{r})\, \epsilon_{\text{xc}}^{\text{LDA}}(n(\boldsymbol{r})), \tag{2.12}$$

where $\epsilon_{\text{xc}}^{\text{LDA}}$ is the energy density of the homogeneous electron gas with density $n(\boldsymbol{r})$ [33, 36]. Valence electrons of solids with nearly free electrons, often behave close to a homogeneous electron gas.

Another family of XC functionals is based on the generalized-gradient approximation (GGA)

$$E_{\text{xc}}^{\text{GGA}}[n] = \int \mathrm{d}\boldsymbol{r}\, n(\boldsymbol{r})\, \epsilon_{\text{xc}}^{\text{GGA}}(n(\boldsymbol{r}), |\nabla n(\boldsymbol{r})|), \tag{2.13}$$

which are semi-local in the sense that they depend on the magnitude of the gradient of the density, i.e., they take into account variations in the immediate surroundings as well as the density itself at a point in space [33, Chapter 8]. Several such functionals exist that rely on different approximations and parametrizations for $\epsilon_{\text{xc}}^{\text{GGA}}$ [40–42].

To accurately account for van-der-Waals interactions from first principles, a non-local XC functional is necessary. Such functionals belong to the family of van der Waals density functionals (vdW-DF) [43–46] and have the general form

$$E_{\text{xc}}^{\text{vdW-DF}}[n] = E_{\text{x}}^{\text{GGA}}[n] + E_{\text{c}}^{\text{LDA}}[n] + E_{\text{c}}^{\text{nl}}[n]. \tag{2.14}$$

The exchange term is thus described by a GGA and the correlation term comprises a local contribution based on the LDA and a non-local contribution

$$E_c^{nl}[n] = \frac{1}{2}\int d\boldsymbol{r}\, d\boldsymbol{r}'\, n(\boldsymbol{r})\, K(\boldsymbol{r},\boldsymbol{r}')\, n(\boldsymbol{r}'), \tag{2.15}$$

where the kernel $K(\boldsymbol{r},\boldsymbol{r}')$ contains information about the strength of the interaction between the density in two points [46, 47]. In this thesis, the vdW-DF-cx functional [45] is used due to its excellent performance for non-magnetic transition metals in general [48], and for the surface properties of Pd, Au, and Cu in particular [49].

2.2 Cluster expansion

Computational studies of alloys require careful consideration of the chemical order. Every possible atomic configuration is associated with its own ground state energy, and to scan through all possible atomic configuration using *ab initio* methods is practically impossible for relevant system sizes. Instead, one has to choose between studying a few selected atomic configurations or turn to simpler models. In this thesis, alloy cluster expansion (CE) models [50] are employed to predict the ordering and segregation of Pd-alloys using the open-source Python package ICET [51]. A CE is a generalized Ising model, which predicts the energy as a function of the atomic configuration on a rigid lattice, based on a decomposition of the occupation vector into atomic clusters [50].

2.2.1 Definitions and formalism

The atomic configuration is described by a configuration vector

$$\boldsymbol{\sigma} = \{\sigma_1, \sigma_2, ..., \sigma_N\}, \tag{2.16}$$

where σ_i represents the occupation of lattice site i and N is the total number of sites. For a binary system consisting of species A and B, σ_i is typically defined as 0 for species A and 1 for species B.

A cluster is defined as a set of k lattice sites. Clusters are classified by their order k and their geometric size which can be defined based on the distances between the sites. Clusters obey the symmetry of the lattice and a group of symmetrically equivalent clusters are said to belong to the same orbit.

For each lattice site i, a set of M point functions $\Theta_n(\sigma_i)$ is defined as

$$\Theta_n(\sigma_i) = \begin{cases} 1, & n = 0 \\ -\cos\left(\frac{\pi(n+1)\sigma_i}{M}\right), & n \text{ odd} \\ -\sin\left(\frac{\pi n\sigma_i}{M}\right), & n \text{ even} \end{cases}$$

where M is the number of allowed species on the site and $n = 0, 1, \ldots, M-1$ is the point function index. The point functions are used to construct a complete, orthogonal basis of the configuration space [52] with basis functions

$$\Pi_{\boldsymbol{\alpha}}(\boldsymbol{\sigma}) = \Theta_{n_1}(\sigma_1)\Theta_{n_2}(\sigma_2)\cdots\Theta_{n_l}(\sigma_l), \tag{2.17}$$

where $\boldsymbol{\alpha} = \{n_1, n_2, \ldots, n_N\}$ is a vector of allowed point function indices for cluster α defined such that n_i represents lattice site i. For a cluster in a binary alloy, n_i takes the value 1 for all sites included in the cluster and 0 otherwise, such that sites not included do not affect the basis function. For more complex systems, such as ternary systems, n_i can take values $1, 2, \ldots M-1$ for sites included in the cluster. The permutation of these leads to multiple basis functions $\Pi_{\boldsymbol{\alpha}}^{(s)}(\boldsymbol{\sigma})$ for each cluster α, where (s) indicates the corresponding point function index. This aspect is, however, beyond the scope of this thesis and the index (s) will not be included in the following.

Any function f of the configuration (such as the energy) can, in principle, be described exactly by

$$f(\boldsymbol{\sigma}) = f_0 + \sum_{\boldsymbol{\alpha}} f_{\boldsymbol{\alpha}}\Pi_{\boldsymbol{\alpha}}(\boldsymbol{\sigma}), \tag{2.18}$$

where $f_{\boldsymbol{\alpha}}$ corresponds to the contribution of each (non-zero order) cluster and f_0 to the configuration independent contribution (the zeroth order cluster) [50]. For symmetry reasons, the sum over all clusters can be reduced to a sum over all orbits where each orbit is represented by one of its clusters $\boldsymbol{\alpha}$ and the basis function is averaged over all clusters $\boldsymbol{\alpha}'$ in the orbit.

$$f(\boldsymbol{\sigma}) = J_0 + \sum_{\boldsymbol{\alpha}} m_{\boldsymbol{\alpha}} J_{\boldsymbol{\alpha}} \langle \Pi_{\boldsymbol{\alpha}'}(\boldsymbol{\sigma}) \rangle_{\boldsymbol{\alpha}}. \tag{2.19}$$

Here, the multiplicity $m_{\boldsymbol{\alpha}}$ of clusters in the orbit represented by $\boldsymbol{\alpha}$ has been introduced and the energetic contributions have been replaced by effective cluster interactions (ECIs) $J_{\boldsymbol{\alpha}}$.

For crystalline materials, where the allowed species differ between sites, such as the hydrides of interest in this thesis, a CE consisting of multiple sublattices can be constructed. This principle can also be used to model surface adsorption. For example, adsorption of H atoms on an alloy surface can be modeled by one surface slab lattice for the alloy and one lattice consisting of the adsorption sites which can be empty or occupied by H.

2.2.2 Cluster expansion construction

A CE is constructed by finding the optimal ECIs based on reference data $\boldsymbol{f} = [f_1(\boldsymbol{\sigma}_1), f_2(\boldsymbol{\sigma}_2), \ldots]^T$ corresponding to a number of selected atomic configurations $\{\boldsymbol{\sigma}_1, \boldsymbol{\sigma}_2, \ldots\}$, The reference data is typically obtained by *ab initio* calculations. Note that

although the CE works on a fixed lattice, the reference data often consists of energy calculations where the cell size and atom positions are fully relaxed. The atom positions are subsequently rescaled and mapped to the fixed lattice to fit the CE. This procedure effectively incorporates relaxation contributions into the lattice model.

To find the optimal ECIs, represented by a vector $\boldsymbol{J} = [J_0, J_1, J_2, ...]^T$, Eq. 2.19 is rewritten as a linear problem

$$\boldsymbol{f} = \boldsymbol{\Pi}\boldsymbol{J}, \tag{2.20}$$

where each row $\boldsymbol{\Pi}_i$ of the sensing matrix $\boldsymbol{\Pi}$ corresponds to the averaged basis function of all orbits multiplied by the respective multiplicity

$$\boldsymbol{\Pi}_i = [1,\ m_{\boldsymbol{\alpha}_1}\langle\Pi_{\boldsymbol{\alpha}_1'}(\boldsymbol{\sigma}_i)\rangle_{\boldsymbol{\alpha}_1},\ m_{\boldsymbol{\alpha}_2}\langle\Pi_{\boldsymbol{\alpha}_2'}(\boldsymbol{\sigma}_i)\rangle_{\boldsymbol{\alpha}_2},\ ...]. \tag{2.21}$$

Here, $\boldsymbol{\Pi}_i$ is referred to as a cluster vector. In practice, the number of orbits included in the CE has to be truncated by introducing an upper limit for the cluster order and size. Equation Eq. 2.20 can be solved for $\boldsymbol{J}$ by linear regression. The simplest approach is to use the ordinary least-squares (OLS) method, which finds the $\boldsymbol{J}$ that minimizes the error of the predicted $\boldsymbol{f}$. OLS is, however, prone to overfitting which can result in unphysical ECIs contributions. To avoid this issue, the reference data set needs to be large compared to the number of ECIs, which is computationally expensive. Another strategy is to use methods which involve regularization and/or feature selection such as recursive feature elimination (RFE), least absolute shrinkage and selection operator (LASSO) [53] or automatic relevance detection regression (ARDR) [54]. These methods result in sparser ECIs ($\boldsymbol{J}$) which typically leads to more stable CEs even for smaller reference data sets.

2.2.3 Exploiting local symmetries

For a bulk binary alloy with a simple face-centered cubic (fcc) structure, the primitive cell consists of a single site. This means that the list of orbits contains one singlet, one nearest neighbor (NN) pair and so on. For a surface slab of the same binary alloy, however, the primitive cell consists of one site per atomic layer. As a result, there are multiple symmetrically inequivalent singlets and NN pairs. For example, the NN pair between layers i and $i + 1$ is not equivalent to the NN pair between layers $i + 1$ and $i + 2$, and as a result they will be represented by different ECIs. Suppose, however, that the slab is very thick and that layer i is far from the surface. In such a case, the behavior of the NN pairs in question should be similar to the single NN from the bulk example.

This principle can be used to define so-called local symmetries for orbits with matching order and radii that should behave similarly. The concept of grouping symmetrically equivalent clusters to the same orbit is extended such that orbits belonging to the same local symmetries are merged and the total number of ECIs is reduced. In Paper I we use

this approach to construct surface CEs for the Pd–Au:H and Pd–Cu:H systems to study surface segregation. We find that merging bulk-like orbits results in models less prone to overfitting that better reproduces the correct segregation behavior.

2.2.4 Training data generation

The predictive ability of a CE is sensitive to the selection of atomic configurations included in the training set. Predictions for configurations poorly represented by the training set will generally be less accurate. In most cases, the accuracy of a CE is increased while the risk of overfitting is reduced with the number of structures in the training data set. Since increasing the size of the training data set typically involves additional costly DFT calculations, a compromise between computational cost and number of structures has to be found.

Many different approaches to structure selection for CEs have been proposed [55–62]. A simple approach is to generate a certain number of random configurations. This will, however, lead to multiple structures with similar cluster vectors (Eq. 2.21) which means that the information provided by additional structures is limited and the numerical problem (Eq. 2.20) is poorly conditioned. For systems with small unit cells, training sets can be constructed by enumerating all inequivalent structures up to a certain structure size [51, 56, 57]. This is, however, not feasible for systems with larger unit cells, since the number of structures produced by enumeration quickly becomes unmanageable. Several approaches are based on identifying structures that are of particular importance for the problem, often in an iterative fashion. That could for example include structures that are close to the ground state [58, 61], structures that minimizes the variance of the predicted property [55, 59, 61] or structures associated with large uncertainties [62]. Another option is to construct a training set where each structure contributes with as much information as possible, by aiming for structures with orthogonal cluster vectors [60]. Nelson *et al.* [60] have developed the following iterative algorithm for this purpose:

1. Generate a random cluster vector.

2. Orthogonalize this vector to the cluster vectors of all previously added structures.

3. Find the structure which most closely matches the current cluster vector and add it to the training set.

This approach was adopted for the surface slab models in Paper I, with some added constraints on the structure cell sizes and target concentrations to avoid ending up with a majority of large structures (for reasons of computational cost) and ensure an even distribution over the concentration range. Due to correlations between the elements

in the cluster vector, it is generally not possible to obtain a sensing matrix with perfectly orthogonal rows, especially not with the added constraints. Nevertheless, this approach has been found to result in accurate models (as demonstrated in Paper I) and is a convenient procedure to generate a training set in one go without having to rely on intermediate CEs.

2.3 Monte Carlo simulation

CEs are often used in combination with Monte Carlo (MC) simulations to obtain thermodynamic information about a system. MC methods represents a broad category of computational algorithms that uses random numbers to calculate deterministic properties [63, Chapter 10]. In the context of modeling alloys, MC simulations and specifically the Metropolis algorithm [64] can be used to efficiently sample the very large configuration space associated with systems large enough to study thermodynamic averages of properties such as free energy, occupancy of specific sites, and order parameters. In the following, this procedure is described.

The probability of a specific atomic configuration $\boldsymbol{\sigma}$ is

$$p(\boldsymbol{\sigma}) = \frac{1}{Z} \exp\left[-\frac{\Phi(\boldsymbol{\sigma})}{k_B T}\right], \tag{2.22}$$

where Z is the partition function, Φ is the thermodynamic potential (excluding the temperature-entropy contribution) associated with the relevant thermodynamic ensemble (see Sect. 2.3.1 and Sect. 2.3.2), k_B is the Boltzmann constant and T is the temperature. A MC simulation starts from a supercell of the system with some arbitrary atomic configuration. In each simulation step, the system is subjected to a trial step where the atomic configuration undergoes some random change, for example swapping the atomic species of two lattice sites. The probabilities (Eq. 2.22) of the atomic configuration before ($\boldsymbol{\sigma}_1$) and after ($\boldsymbol{\sigma}_2$) the swap are compared. If the ratio between the latter and the former is larger than a uniform random number $\xi \in (0, 1)$,

$$\frac{p(\boldsymbol{\sigma}_2)}{p(\boldsymbol{\sigma}_1)} > \xi, \tag{2.23}$$

the new configuration ($\boldsymbol{\sigma}_2$) is accepted, otherwise the system remains in the old configuration ($\boldsymbol{\sigma}_1$). Note that the partition function Z never has to be calculated explicitly. With this algorithm, a lower energy configuration is always accepted while higher energy configurations are sometimes accepted, which allows for an exploration of more probable configurations without getting stuck in local minima. The value of any quantity of interest is saved for every simulation step and since the configuration space is sampled according to the probability Eq. 2.22, the resulting averages correspond to ensemble averages.

The choice of thermodynamic ensemble, which determines the thermodynamic potential in Eq. 2.22, depends on the properties of the system. For example, an isolated system with constant number of particles, volume, and energy is described by the microcanonical ensemble. In the microcanonical ensemble, a macrostate is defined by the values of the constant macroscopic variables N, V, E. A macrostate generally corresponds to multiple microstates with varying probabilities. During a MC simulation, the system changes between different microstates while remaining in the same macrostate. In the following, two thermodynamic ensembles relevant for this thesis are presented.

2.3.1 The canonical ensemble

The canonical ensemble represents a system at constant volume V with a fixed number of atoms of each species N_i (where i is the atomic species) in contact with an infinite reservoir at constant temperature T. A macrostate in the canonical ensemble is thus described by (N_i, V, T). The thermodynamical potential, which determines the probability of a microstate, corresponds to the internal energy.

In this thesis, the internal energy is represented by the configurational energy predicted by the CEs while other contributions, such as vibrations, are neglected. The microstate is then determined by the atomic configuration $\boldsymbol{\sigma}$ and the probability is

$$p_{\mathrm{C}}(\boldsymbol{\sigma}) = \frac{1}{Z} \exp[-\frac{E(\boldsymbol{\sigma})}{k_B T}], \tag{2.24}$$

where E is the configurational energy. Since the numbers of particles of each species are constant, the atomic concentrations are fixed and a suitable trial step consists of swapping the species of two sites.

2.3.2 The semi-grand canonical ensemble

In the semi-grand canonical (SGC) ensemble, the total number of atoms N, the volume V and the temperature T are constant. The difference to the canonical ensemble is that the number of atoms per specie, N_i, can vary (under the condition that $N = \sum_i N_i$) and instead, the chemical potential difference $\delta\mu_i = \mu_1 - \mu_i$ for each species $i > 1$ in relation to the first species is constant [65]. Fixing the chemical potential difference effectively controls the average concentrations during a MC simulation. The SGC ensemble thus represents a system in contact with an infinite reservoir with fixed temperature and chemical potential differences, such that both energy and atoms can be exchanged and a macrostate is described by $(N, \Delta\mu_i, V, T)$.

Within the scope of this thesis, the probability of a microstate in the SGC ensemble is defined as

$$p_{\mathrm{SGC}}(\boldsymbol{\sigma}) = \frac{1}{Z} \exp[-\frac{E(\boldsymbol{\sigma}) + \sum_{i>1} \Delta\mu_i N_i}{k_B T}], \tag{2.25}$$

where E is the configurational energy obtained from a CE and the second term is associated to the potential energy related to the chemical potentials. A trial step consists of changing the species of one site.

The SGC ensemble has two main advantages over the canonical ensemble. First, the control of $\delta_m u_i$ allows for efficient sampling over the entire concentration range and the free energy can be obtained by integration of the thermodynamic relation

$$\Delta\mu_i = -\frac{1}{N}\frac{\partial F}{\partial c_i}, \tag{2.26}$$

which is convenient for, e.g., phase diagram construction. Second, for gas adsorption/absorption, knowledge of the chemical potential $\mu_i(T, p_i)$ means that the corresponding partial pressure p_i can be calculated via

$$\mu_i(T, p_i) = \mu_i^\circ(T) + k_B T \ln \frac{p_i}{p_i^\circ}, \tag{2.27}$$

where $\mu_i^\circ(T)$ is the temperature dependent chemical potential of the gas at a reference pressure p_i°. This relation is used in Paper I to connect the segregation behavior of Pd-alloys to the hydrogen pressure.

2.3.3 Simulated annealing

In addition to calculating ensemble averages of quantities of interest, MC simulations can be used to simulate an annealing process for alloys. The simulated annealing procedure is similar to a regular MC simulation, with the difference that the temperature is gradually decreased during the simulation and the most important result is the end configuration [66]. The ratio of accepted trial steps increases with temperature, which means that the system can move further away from the ground state during the simulation. As the temperature is reduced, the acceptance ratio decreases and the system becomes gradually more locked in to a specific low energy configuration. The end configuration is typically a good estimation of the lowest energy configuration at the end temperature, which is close to the ground state for sufficiently low temperatures. Simulated annealing can be used to, e.g., identify low energy structures for training data generation (Sect. 2.2.4) or study atomic ordering.

2.4 Electrodynamic simulations

To study the optical response of NPs with diameters on the order of 100 nm, continuum electrodynamic simulations on a macroscopic scale are necessary, in contrast to the atomistic methods previously discussed in this chapter. Such simulations typically

involve solving Maxwell's equations. The time-dependent macroscopic Maxwell equations in differential form (without electric or magnetic current sources) read [67, Chapter 3]

$$\frac{\partial \boldsymbol{D}}{\partial t} = \nabla \times \boldsymbol{H} - \boldsymbol{J} \tag{2.28}$$

$$\frac{\partial \boldsymbol{B}}{\partial t} = -\nabla \times \boldsymbol{E} - \boldsymbol{M} \tag{2.29}$$

$$\nabla \cdot \boldsymbol{D} = 0 \tag{2.30}$$

$$\nabla \cdot \boldsymbol{B} = 0 \tag{2.31}$$

where $\boldsymbol{E}$ is the electric field, $\boldsymbol{D}$ is the electric displacement field, $\boldsymbol{H}$ is the magnetic field, $\boldsymbol{B}$ is the magnetic flux density, $\boldsymbol{J}$ is the electric current density and $\boldsymbol{M}$ is the magnetic current density. The fields (excluding $\boldsymbol{J}$‘ and $\boldsymbol{M}$) are related by the following constitutive relations

$$\boldsymbol{D} = \varepsilon \boldsymbol{E} \tag{2.32}$$

$$\boldsymbol{B} = \mu \boldsymbol{H}, \tag{2.33}$$

where ε is the electrical permittivity and μ is the magnetic permeability. The current densities can include both independent sources ($\boldsymbol{J}_\mathrm{s}$ and $\boldsymbol{M}_\mathrm{s}$) and nondispersive losses via the electric and magnetic conductivities (σ and σ^*),

$$\boldsymbol{J} = \boldsymbol{J}_\mathrm{s} + \sigma \boldsymbol{E} \tag{2.34}$$

$$\boldsymbol{M} = \boldsymbol{M}_\mathrm{s} + \sigma^* \boldsymbol{H}. \tag{2.35}$$

The material properties are included via ε, μ, σ, and σ^* which may vary over the simulation region to simulate specific objects. In this thesis, non-magnetic ($\mu = 1, \sigma^* = 0$) materials are considered. The material specific property of interest is thus the permittivity (ε), which can be complex and frequency dependent (dispersive). For dispersive materials, the permittivity is often called the DF. The DF for an arbitrary alloy is generally not known but can be calculated using *ab initio* methods as outlined in Ref. [68]. This approach was adopted in Paper II to obtain DFs for the Pd–Au–H system but is outside the scope of this thesis.

There are many different approaches to solving Maxwell's equations numerically. In this thesis, the simple yet powerful finite-difference time-domain (FDTD) method is used as implemented in the open-source software MEEP [69].

2.4.1 Finite-difference time-domain method

The FDTD method is based on solving the system of six partial differential equations formed by Eq. 2.29 and Eq. 2.28 by evolving them in time. The method is typically im-

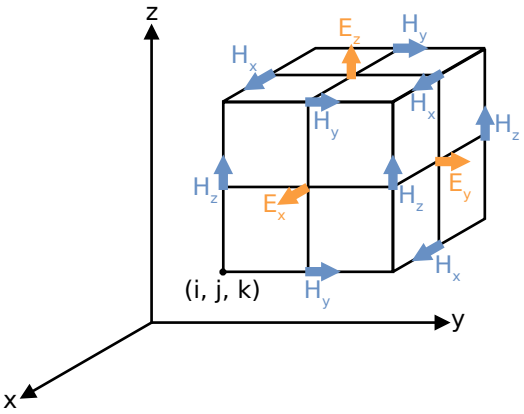

Figure 2.1: Illustration of the Yee grid.

plemented on a Yee grid [70] where the $\boldsymbol{E}$ and $\boldsymbol{H}$-field components are placed on a staggered grid in three dimensional space with an offset of half a pixel, such that each $\boldsymbol{E}$-field component is encircled by four perpendicular $\boldsymbol{H}$-field components and vice versa, as shown in Fig. 2.1. This scheme is convenient since it allows for center-difference derivatives with second order accuracy, enforces continuity of tangential $\boldsymbol{E}$-fields and normal $\boldsymbol{H}$-fields at surfaces and implicitly enforces Eq. 2.30 and Eq. 2.31 [67, Chapter 3]. Similarly, the evolution in time follows a leapfrog arrangement where the $\boldsymbol{E}$- and $\boldsymbol{H}$-field components are separated in time by half a time step. As a result, the time evolution is fully explicit and the involved time derivatives are also central-differences with second-order accuracy. In general, the Yee grid is cubic and characterized by a resolution $\Delta x = \Delta y = \Delta z = \Delta$ much smaller than the wavelength [70]. To achieve numerical stability, the resolution in time must fulfill the Courant condition [67, Chapter 4]

$$\Delta t < \frac{\Delta}{c\sqrt{3}} \text{ (in 3D).} \tag{2.36}$$

A FDTD simulation takes place in a finite computational cell truncated by some boundary condition. A common choice for non-periodic systems is to surround the computational cell with a perfectly matched layer (PML) layer. A PML layer is a fictitious material designed to absorb all incoming fields with no reflection [67, Chapter 7]. This setup is equivalent to simulating the system in an infinite cell with no reflecting structures beyond the computational cell.

In the following, the implementation of a FDTD method on a Yee grid is briefly covered based on Ref. [67, Chapter 3]. Any function u of space and time is denoted using the following notation

$$u(i\Delta x, j\Delta y, k\Delta z, n\Delta t) = u^n_{i,j,k} \tag{2.37}$$

and is associated with the following central differences in space (represented by the x-

direction) and time

$$\frac{\partial u^n_{i,j,k}}{\partial x} = \frac{u^n_{i+1/2,j,k} - u^n_{i-1/2,j,k}}{\Delta x} + \mathcal{O}[(\Delta x)^2] \tag{2.38}$$

$$\frac{\partial u^n_{i,j,k}}{\partial t} = \frac{u^{n+1/2}_{i,j,k} - u^{n-1/2}_{i,j,k}}{\Delta t} + \mathcal{O}[(\Delta t)^2]. \tag{2.39}$$

The first of the six partial differential equations (Eq. 2.28 in x-direction) reads (using Eq. 2.32):

$$\frac{\partial E_x}{\partial t} = \frac{1}{\varepsilon}\left[\frac{\partial H_z}{\partial y} - \frac{\partial H_y}{\partial z} - J_x\right], \tag{2.40}$$

where Eq. 2.32 is used to obtain an equation in E_x instead of D_x. Rewriting this equation in terms of central differences yields

$$\begin{aligned}\frac{E_x\big|^{n+1/2}_{i,j+1/2,k+1/2} - E_x\big|^{n-1/2}_{i,j+1/2,k+1/2}}{\Delta t} = \frac{1}{\varepsilon}\Bigg[&\frac{H_z\big|^{n}_{i,j+1,k+1/2} - H_z\big|^{n}_{i,j,k+1/2}}{\Delta y} + \dots \\ &+ \frac{H_y\big|^{n}_{i,j+1/2,k+1} - H_y\big|^{n}_{i,j+1/2,k}}{\Delta z} - J_x\big|^{n}_{i,j+1/2,k+1/2}\Bigg].\end{aligned} \tag{2.41}$$

During time evolution, the term $E_x\big|^{n+1/2}_{i,j+1/2,k+1/2}$ is calculated as a function of the other terms which are known since they belong to earlier time steps. The procedure is equivalent for the remaining 5 partial differential equations and will result in the calculation of $\boldsymbol{E}$ at half integer time steps $(n + 1/2)$ and $\boldsymbol{H}$ at integer time steps $(n + 1)$.

For dispersive materials, i.e., materials with a frequency dependent permittivity, the algorithm has to be modified slightly. The electric displacement field can be written as

$$\boldsymbol{D} = \varepsilon \boldsymbol{E} = \varepsilon_0 \boldsymbol{E} + \boldsymbol{P}, \tag{2.42}$$

where $\boldsymbol{P}$ is the induced polarization. The physical origin of dispersion is a time delay of the induced polarization in response to an electric field. The effect of dispersion can thus be implemented in a FDTD algorithm by accounting for the time evolution of $\boldsymbol{P}$. This can be achieved by the auxiliary differential equation method [67, Chapter 9]. Given an analytical expression for the DF $\varepsilon(\omega)$, such as the Lorentzian representation used in Paper II, the polarization field can be related to the electric field in frequency space

$$\boldsymbol{P}(\omega) = [\varepsilon(\omega) - \varepsilon_0]\, \boldsymbol{E}(\omega). \tag{2.43}$$

By performing an inverse Fourier transform, a differential equation for the time evolution of $\boldsymbol{P}$ is obtained, which can be solved numerically with finite differences alongside

Maxwell's equations. Lastly, Eq. 2.40 is modified according to

$$\frac{\partial E_x}{\partial t} = \frac{1}{\varepsilon_\infty}\left[\frac{\partial H_z}{\partial y} - \frac{\partial H_y}{\partial z} - J_x - P_x\right], \tag{2.44}$$

where P_x is the x-component of the polarization obtained from the auxiliary differential equation (which typically involves additional E_x-terms).

3

Thermodynamics of hydrogenated Pd-alloys

The first key property of Pd-nanoalloys that enables H sensing is their ability to quickly undergo absorption or desorption of large quantities of H, in relation to the concentration of H_2 in the immediate environment. This is possible due to the thermodynamics of the Pd–H system, which dictates that H absorption is energetically favorable already at fairly low H_2 pressures (~10 mbar at room temperature [71]). Alloying with other metals introduces tunability of the material properties and is a common strategy for material optimization in various applications. This strategy requires knowledge about how the introduction of additional species affects the thermodynamics of the system, with regard to e.g. H absorption and chemical order in the metal lattice. In this section, the thermodynamics of hydrogenated Pd-alloys is discussed with emphasis on the effects of alloying and surface segregation.

3.1 Bulk properties

According to the laws of thermodynamics, a system strives towards the state with lowest Gibbs free energy,

$$G = U + PV - TS. \tag{3.1}$$

For alloys and metal-H systems in bulk, this principle can be used to construct phase diagrams where the equilibrium phase(s) of a material is mapped out as a function of composition and temperature (at constant pressure).

To understand the free energy of a multicomponent system, we first need to consider the change in free energy during mixing [72, Chapter 5]. Consider a system consisting of two subsystems with atom species A or B at constant temperature (T) and pressure

(P) that are initially separated (unmixed). The corresponding free energy for, say, one mole of the total system is

$$G_{\text{unmix}} = (1 - x)G_A + xG_B, \tag{3.2}$$

where x is the fraction of B atoms and G_A, G_B are the free energies of one mole of A and B atoms, respectively. If the separation between the subsystems is removed, they will mix if the change in free energy upon mixing is negative.

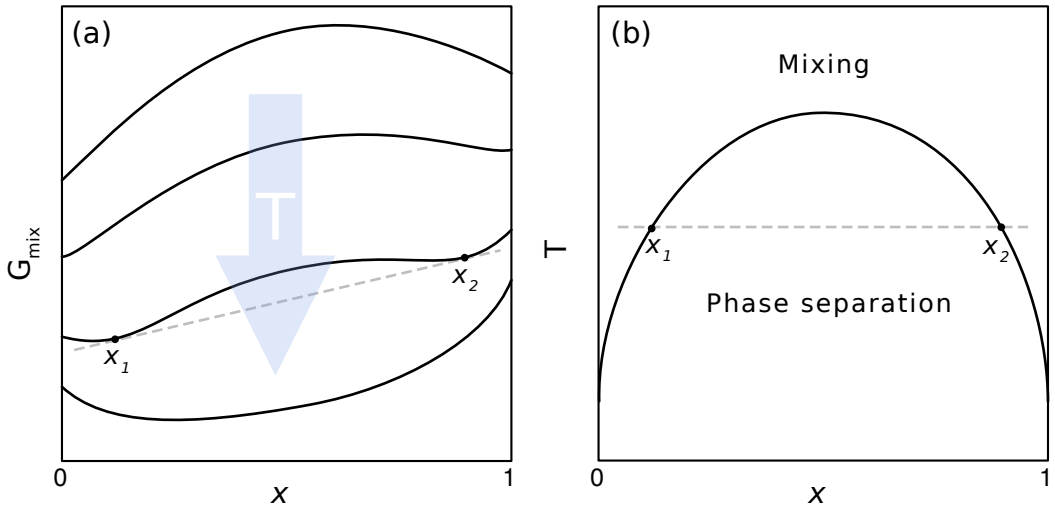

Figure 3.1: Schematic illustration of the Gibbs free energy for a mixed system consisting of atoms A and B (a) and the corresponding phase diagram (b). If any part of the Gibbs free energy curve is concave-up, the system will separate into two phases with compositions $x_1(T)$, $x_2(T)$ in this region. The Gibbs free energy of the phase separated system will follow the tangent below the curve (dashed line), which guarantees a lower energy compared to a mixed system which would follow the curve (solid line). If the entire curve is concave-up, no mixing occurs and the Gibbs free energy of the system is given by Eq. 3.2.

During mixing, the internal energy U may decrease or increase depending on the interactions between A and B atoms. Similarly, the volume V may change, but the effect on the change in free energy is generally small for solids. The entropy S, however, will always increase upon mixing due to the increased number of ways to arrange the atoms in a mixed system. Whether or not the subsystems will mix at a certain temperature thus primarily depends on the sign and amplitude of the change in internal energy ΔU_{mix} upon mixing. If $\Delta U_{\text{mix}} < 0$, the system will mix at all temperatures since both the internal energy and entropy contributions to the free energy is reduced. If $\Delta U_{\text{mix}} > 0$, on the other hand, the system will mix above the temperature at which the magnitude of the entropy contribution is larger than the internal energy contribution. Below this

temperature, the system will phase separate into one A-rich and one B-rich phase, as shown in Fig. 3.1.

3.1.1 The Pd–H system

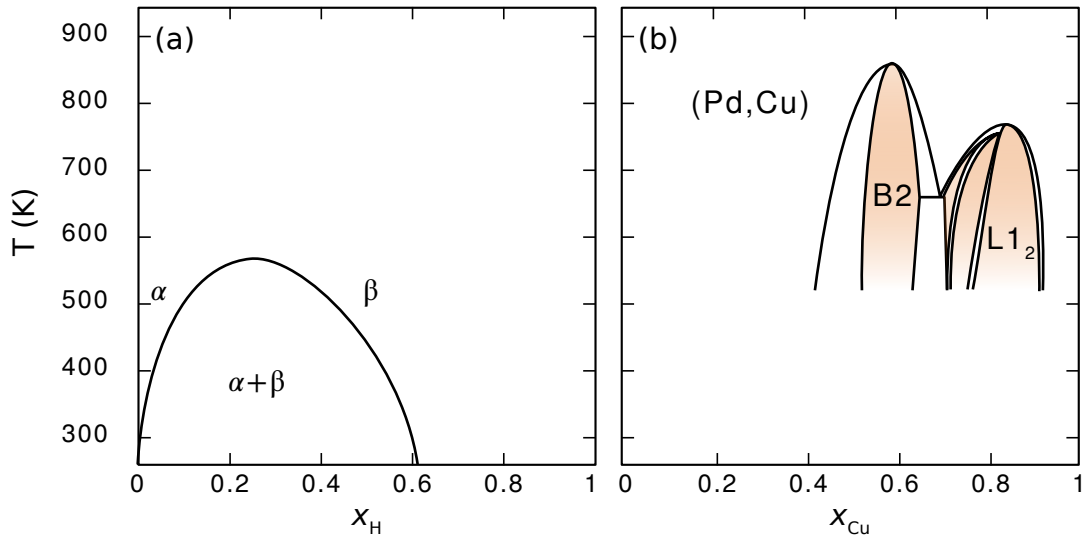

Figure 3.2: (a) Phase diagram for solid Pd–H adapted from [73]. PdH exhibits two phases with the same crystal structure, α and β, which causes phase separation at temperatures below approximately 600 K. (b) Phase diagram for solid Pd–Cu adapted from [74]. The Pd–Cu system is mostly miscible (Pd, Cu) but have several ordered phases in the Cu-rich end (orange regions) which causes phase separation (white areas next to an orange area).

The H absorption process in Pd begins with dissociation of H_2 molecules into atomic H at the metal surface. When the surface is covered by one monolayer, the H atoms move to interstitial sites in the Pd lattice forming an interstitial alloy. The alloy remains metallic due to the similar electronegativities of Pd and H atoms [75, Chapter 2]. The first step is associated with a decrease in energy, which is followed by an increase in energy in the second step, but absorption to the bulk is still energetically favorable compared to the H_2 gas phase (Fig. 3.3d).

H absorption is associated with an expansion of the Pd lattice. At moderate temperatures ($\lesssim$ 600 K), this causes a phase separation between the H-poor α-phase and the H-rich β-phase as the H content increases (Fig. 3.2a). In experiments and applications, the absorbed H content vs. H_2 pressure at a fixed pressure is often of interest. Due to the phase separation, such a measurement is associated with a jump from low to high H content at the so-called plateau pressure and hysteresis caused by the energy barriers of forming β in α and vice versa [73]. These phenomena are often unwanted, for example

in H sensing, since the H content is not a well-defined or strictly monotonic function of H_2 pressure.

3.1.2 Alloying with Au or Cu

Solid Pd–Au alloys are miscible over the entire composition range [76]. Some ordered phases have been observed, but these do not cause significant phase separation and there is a lack of consensus in the literature [76]. Alloying Pd with Au is often beneficial in H applications since the miscibility gap and hysteresis (characteristic for the Pd–H system) vanish at approximately 15% Au [28, 77]. This effect is mainly due to the larger size of Au atoms compared to Pd, which causes a lattice expansion similar to the expansion needed to absorb large quantities of H [75, Chapter 3]. At the same time, the H solubility reduces roughly linearly with Au content. For example, at 30% Au content the solubility of H_2 at 1 bar is about 25% compared to 67% for pure Pd [28].

Solid Pd–Cu alloys are completely miscible for compositions with more than 60% Pd (Fig. 3.2b), which are the primary focus of this thesis. For higher Cu content, however, several ordered phases can be found which causes phase separation. This includes the B2-phase close to 50% Cu with different crystal structure (CsCl structure) than the solid solution (Pd,Cu) which causes difficulties in modeling with lattice-based methods such as CEs. Since the Cu atom is smaller than Pd, alloying with Cu does not have the same benefits as alloying with Au when it comes to the miscibility gap associated with H absorption. Similar to alloying with Au, however, the H solubility decreases with increased Cu content [78].

3.2 Surface properties

The energy landscape of an atom close to a surface differs from an atom in the bulk due to the change in coordination number, surface relaxation, and possible interaction with adsorbates. This is also true for atoms close to surfaces with different orientations. The energy difference gives rise to the concept of surface energy, i.e., the energy per area required to form a surface (of a certain orientation) by splitting a bulk material. A lower surface energy means a more stable surface, and a surface slab or the facets of a NP are more likely to have the surface orientation(s) with lowest energy [79]. In Fig. 3.3a, the calculated fcc surface energies for Pd, Au and Cu in the {111}, {100}, and {110} directions as well as experimentally measured facet-averaged surface energies for droplets [80] are displayed. The {111} surface is the most stable one in all cases, with the lowest surface energy for Au followed by Cu and then Pd.

For an alloy, the different energy landscape generally results in a different chemical order of atoms close to the surface compared to bulk. This gives rise to phenomena such as surface segregation and surface ordering. These phenomena have a large impact

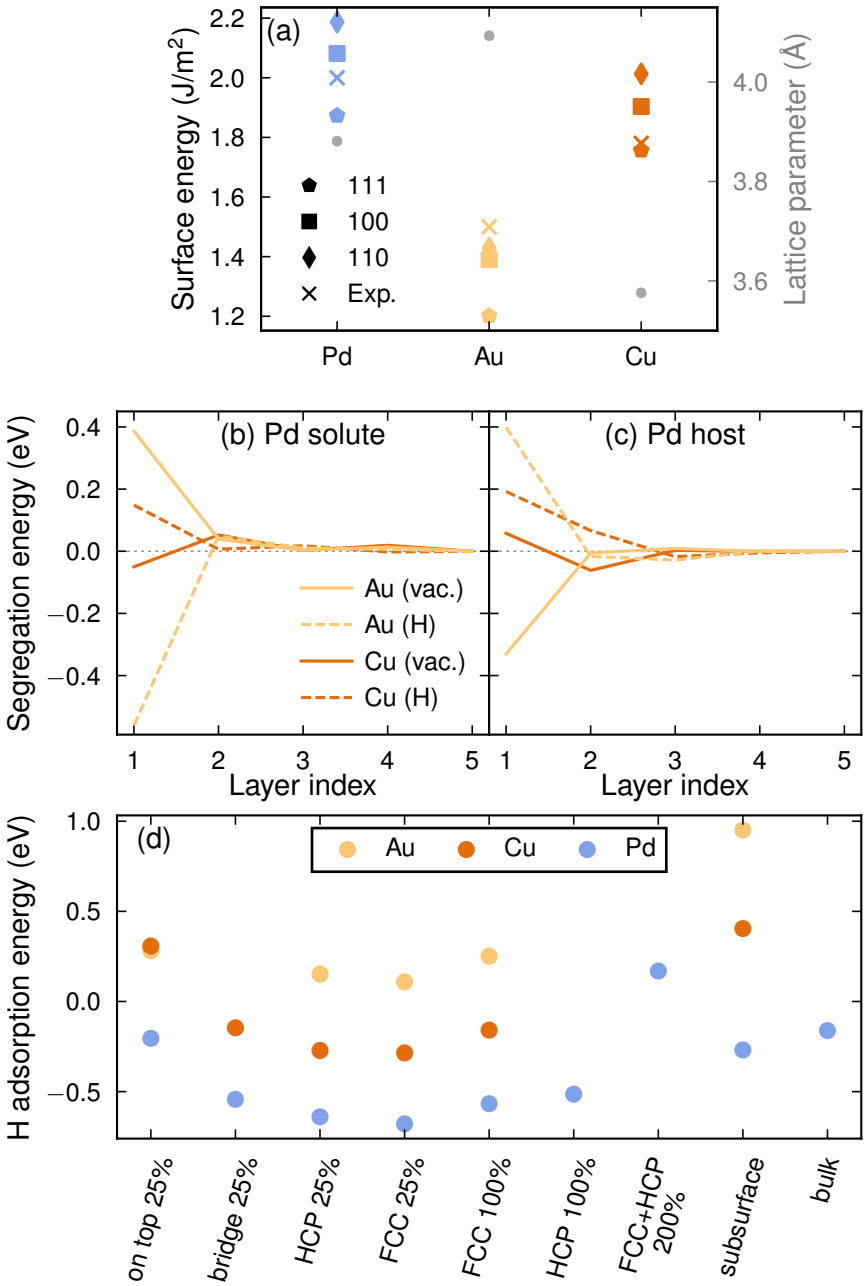

Figure 3.3: (a) Surface energies for different orientations and experimental measurements from [80] as well as the bulk lattice parameter (in grey). (b-c) Segregation energies for fcc-{111} slabs with Pd as the solute (b) or host (c) species, in vacuum or with 100% H coverage. (d) Adsorption energies for H sites on fcc-{111} slabs, where the occupation is provided on the x-axis in terms of H per surface atom. All energies are calculated using DFT with the vdW-DF-cx functional. The surface energies were calculated in [49] and the segregation and adsorption energies in Paper I.

on the surface properties and are crucial for the performance in applications such as catalysis and sensing, for which the composition of the top-most surface layers is crucial. The surface segregation behavior of an arbitrary alloy is generally hard to predict since it requires knowledge about the energy of all possible atomic configurations. There are, however, some general properties that typically induce surface segregation that can be identified from modeling of segregation in a dilute alloy $A_x B_{1-x}$ consisting of a single A (solute) atom in B (host) [81–84]:

- **Pure metal surface energy**: The species with lower surface energy tend to segregate towards the surface. This is generally considered the strongest indication of surface segregation.
- **Size-mismatch**: If there is a large size difference between the solute and host, the solute tends to segregate to the surface [82], at least if it is larger [84, 85].
- **Adsorption energies** (if adsorbates are involved): The species with lower adsorbate energy tends to segregate to the surface [86].

A more quantitative approach is to calculate the segregation energy E^{seg} using *ab initio* calculations,

$$E_x^{\text{seg}} = E_{\text{A in } x} - E_{\text{A in bulk}}, \tag{3.3}$$

where the energies on the right-hand side are calculated for a single A atom in layer x and for a single A atom in bulk.

3.2.1 Surface segregation in Pd–Au–H

A pure, clean Au surface slab has significantly lower surface energy compared to Pd and has a larger lattice parameter (Fig. 3.3a). Both of these factors indicate segregation of Au to the surface in a Pd–Au alloy. Segregation energy calculations further show that, in vacuum, a single Pd atom in Au tends to stay away from the surface (Fig. 3.3b) while a single Au atom in Pd prefers residing at the surface (Fig. 3.3c), i.e. segregation of Au to the surface in both dilute limits. This is also what is generally observed in the literature for Pd–Au surfaces in vacuum [87–95].

The H adsorption energy, on the other hand, is significantly lower on Pd compared to Au (Fig. 3.3d) which indicates segregation of Pd to the surface. Indeed, this effect is strong enough to completely flip the segregation energies in the dilute limits (Fig. 3.3b,c) when a monolayer of H is adsorbed compared to clean surfaces in vacuum. We thus expect surface enrichment of Pd in a H environment, which is also in accordance with the literature [92, 94, 96, 97].

Our findings regarding the surface segregation of Pd–Au surfaces in Paper I, where we study the surface composition as a function of the H_2 pressure, are in agreement with the indications and previous results presented in this section.

3.2.2 Surface segregation in Pd–Cu–H

For the Pd–Cu system, the segregation behavior is harder to predict. The surface energy is lower for a clean Cu surface compared to Pd, but the difference is small (Fig. 3.3a). Furthermore, the lattice parameter is smaller for Cu which indicates segregation of Pd in Cu, in contrast to the surface energy (Fig. 3.3a). The magnitude of the corresponding segregation energies in vacuum is significantly smaller than for the Pd–Au system and shows an oscillatory behavior where Pd is preferred at the topmost surface layer and Cu in the subsequent layer (Fig. 3.3b-c).

The somewhat conflicting indications for Pd–Cu alloys in vacuum are accompanied by an apparent discrepancy in the literature. Many experimental studies find Pd enrichment in the surface region (~6 layers), but Cu enrichment in the topmost surface layer(s) [98–100]. Computational work by Cheng *et al.* [101] supports these findings. Many theoretical studies, however, report the opposite behavior with a slight enrichment in the topmost surface layer [87, 88, 94, 95], at least for low Cu concentrations [92, 102]. Furthermore, experimental work by Pielsticker *et al.* [103] shows that Pd deposited on Cu surfaces in the {111} (but not {110} or {100}) direction in vacuum avoids alloying, suggesting that Pd prefers residing at the surface. Generally, many studies mention oscillatory segregation behavior [88, 101, 104] and a strong orientation dependence [103, 104].

The H adsorption energy is lower on Pd than Cu (Fig. 3.3d). For Pd-rich surfaces, this leads to an increased tendency for Cu to avoid the surface, extending to the second surface layer (Fig. 3.3c). Surprisingly, for Cu-rich surfaces the segregation energy is, however, flipped by the adsorption of H such that Pd tends to avoid the topmost surface layer. This behavior contradicts all of the general indications for surface segregation. For the purpose of this thesis, the primary focus is, however, on materials consisting of at least 50% Pd. The literature includes findings of a general Pd enrichment at the surface [92], Pd enrichment at the surface for low Cu concentration [105] and Pd depletion at the surface for high Cu concentrations [103, 106] in a hydrogen environment.

The discrepancy regarding the segregation behavior for Pd–Cu surfaces is primarily between experimental and theoretical studies. Although it is hard, if not impossible, to find the underlying cause, there are some hypotheses. First, on the experimental end, it is possible that the sensitivity of the experimental methods (typically low energy ion scattering (LEIS) and X-ray photoelectron spectroscopy (XPS) is insufficient to accurately measure the layer-by-layer resolved segregation behavior. Due to the oscillatory behavior and the Cu enrichment in layer 2, the resolution of individual layers is crucial to obtain correct results. Second, computational approaches (including the work in this thesis) typically involve calculations of fcc-{111} surfaces which might not be an accurate representation of the experimental systems, especially given the strong dependence on surface direction. Third, even if the theoretical work is based on *ab initio* calculations, they are only as accurate as the inherent approximations (namely, the exchange-correlation functional in DFT calculations). Fig. 3.3a indicates that using the

vdW-DF-cx functional, the surface energy is underestimated for Pd relative to Cu, which might exaggerate the tendency for Pd to segregate to the surface.

Our findings in Paper I are in line with most theoretical findings, with Pd enrichment at the surface in vacuum and at moderate H_2 pressures for up to 50% Cu (in the bulk). In addition, our findings present an alternative possible explanation to the Pd–Cu discrepancy. At very low H_2 pressures, below or similar to the ultra-high vacuum (UHV) conditions typically used in experiments, there is a local maximum in Cu surface concentration, different from the behavior in the total absence of H. This finding highlights the non-trivial relation between H_2 pressure and the surface state of Pd–Cu alloys and could mean that the behavior in experimental UHV conditions is not equal to the behavior in true vacuum.

4

Optical properties of hydrogenated Pd-alloys

The second key property of Pd-nanoalloys enabling H sensing is the fact that their optical response changes with H uptake. In this chapter, the classical theory behind the optical response of metal nanostructures is reviewed (based on [107]), including a discussion of LSPRs and the DF. In the last section, these concepts are applied to hydrogenated Pd-alloys based on the findings in Paper II.

4.1 Localized surface plasmon resonance

A plasmon is a collective oscillation of free electrons, excited by an external electrical field. In a NP, the confinement in space gives rise to a special kind of plasmon, a localized surface plasmon, where the free electrons move from one side of the NP to the opposite, resulting in an oscillating internal field.

The LSPR can be described using classical theory. First, we define the polarizability $\alpha(\omega)$ of a material

$$\alpha(\omega) = \frac{\boldsymbol{P}(\omega)}{\boldsymbol{E}(\omega)}, \tag{4.1}$$

where $\boldsymbol{E}$ is the total electric field and $\boldsymbol{P}$ is the induced dipole moment. According to Mie theory, a small sphere (in comparison to the wavelength) in vacuum has the polarizability [107, Chapter 5]

$$\alpha(\omega) = 3\varepsilon_0 V \frac{\varepsilon(\omega) - 1}{\varepsilon(\omega) + 2}, \tag{4.2}$$

where $\varepsilon(\omega)$ is the DF of the sphere. From the polarizability, the absorption and scattering cross sections are obtained as

$$\sigma_{\text{abs}}(\omega) = \frac{\omega}{\varepsilon_0 c} \operatorname{Im} \alpha(\omega) \tag{4.3}$$

$$\sigma_{\text{sca}}(\omega) = \frac{1}{6\pi\varepsilon_0^2} \left(\frac{\omega}{c}\right)^4 |\alpha(\omega)|^2, \tag{4.4}$$

which gives the total extinction cross section

$$\sigma_{\text{ext}}(\omega) = \sigma_{\text{abs}}(\omega) + \sigma_{\text{sca}}(\omega). \tag{4.5}$$

The LSPR corresponds to the maximum in extinction or equivalently, the maximum in polarizability. Provided that $\operatorname{Im} \varepsilon(\omega)$ is small or at least slowly varying, the resonance condition reads

$$\operatorname{Re} \varepsilon(\omega) = -2. \tag{4.6}$$

Note that the amplitude of the polarizability, and in turn the LSPR, increases with the NP volume.

A similar description can be derived for small ellipsoids. For an ellipsoid with semiaxes a_x, a_y, a_z, the polarizability in a field parallel to one of its principal axes a_i is [107, Chapter 5]

$$\alpha_i(\omega) = 3\varepsilon_0 V \frac{\varepsilon(\omega) - 1}{L_i(\varepsilon(\omega) - 1) + 1}, \tag{4.7}$$

where L_i is the geometrical factor

$$L_i = \frac{a_x a_y a_z}{2} \int_0^\infty \frac{dq}{(a_i^2 + q)\sqrt{(a_x^2 + q)(a_y^2 + q)(a_z^2 + q)}}, \tag{4.8}$$

which fulfills the relation

$$L_x + L_z + L_y = 1. \tag{4.9}$$

By maximizing the polarizability, the resonance condition for an ellipsoid is obtained as

$$\operatorname{Re} \varepsilon(\omega) = -\frac{1}{L_i} + 1. \tag{4.10}$$

Note that for a sphere, the geometrical factors are all equal and $L_i = \frac{1}{3}$ in which case Eq. 4.10 is reduced to Eq. 4.6.

The resonance condition for ellipsoids (Eq. 4.10) implies that the resonance frequency depends on the size of the appropriate geometrical factor L_i which, in turn, depend on the relationship between the semiaxes. For the purpose of this thesis, we are interested in nanodisks, which are similar to an oblate spheroid ($a_x = a_y = a_{xy} > a_z$), where the

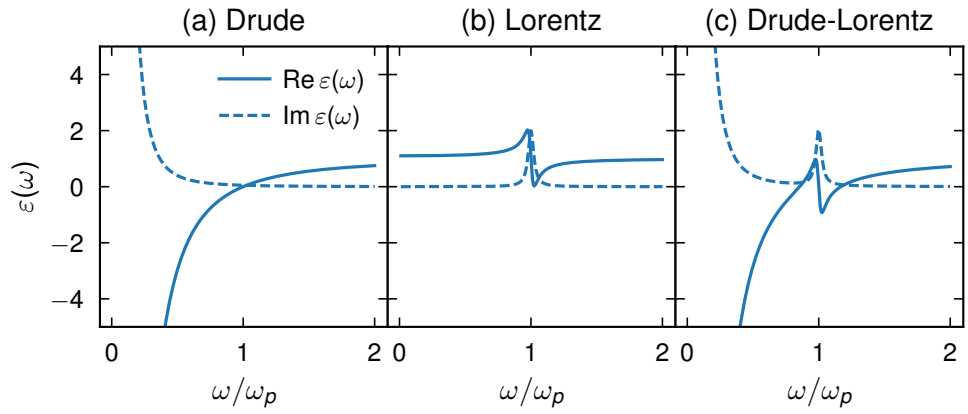

Figure 4.1: DFs according to the (a) Drude, (b) Lorentz and (c) Drude-Lorentz models. The resonance frequency ω_0 for the Lorentz and Drude-Lorentz case coincides with the plasma frequency.

incoming field is parallel to the xy-plane. In this case, the relevant geometrical factor is $L_x = L_y = L_{xy}$. The geometrical factor L_i decreases as the semiaxis a_i increases which implies that $L_{xy} < \frac{1}{3}$ according to Eq. 4.9. As a result, the resonance condition Eq. 4.10 shifts to more negative values of Re $\varepsilon(\omega)$ as the spheroid aspect ratio $\frac{a_{xy}}{a_z}$ increases.

Although the results above are not strictly valid for many real nanoplasmonic systems due to larger size or more complicated geometries, they are a good starting point to gain intuition about the general behavior of the LSPR peak. Most importantly, the fact that the LSPR peak is expected to shift with increased aspect ratio.

4.2 The dielectric function

The connection between a material and its optical properties is the DF. If measured experimentally or calculated using *ab initio* methods, all relevant quantum effects, such as electronic transitions, are included in the DF. The resulting DF can be applied in e.g. Mie theory or electrodynamic simulations (such as FDTD simulations, Sect. 2.4) to study macroscopic optical properties. To gain a qualitative understanding of the connection between the DF and the underlying physical phenomena, classical models of the DF are very useful. For the scope of this thesis, i.e. Pd-alloy hydrides, the Drude and Lorentz models are of particular importance.

The Drude model [107, Chapter 9]

$$\varepsilon(\omega) = 1 - \frac{\omega_p^2}{\omega^2 + i\gamma\omega}, \tag{4.11}$$

where ω_p^2 is the plasma frequency (corresponding to the bulk plasmon) and γ is a damping constant, models the optical properties of a free-electron metal (Fig. 4.1a). A Drude-like metal is highly reflective at frequencies below the plasma frequency, which typically includes the visible spectra. Above the plasma frequency, the DF approaches the permittivity of vacuum and the metal becomes transparent.

The Lorentz model [107, Chapter 9]

$$\varepsilon(\omega) = 1 + \frac{\omega_p^2}{\omega_0^2 - \omega^2 - i\gamma\omega} \tag{4.12}$$

models the optical properties of a harmonic oscillator with resonance frequency ω_0, where the oscillator represents a bound electron or an ion (Fig. 4.1b). A Lorentz-type material has an increase in reflectance close to the resonance frequency due to increased absorption and behaves like vacuum far from the resonance frequency. Note that if the resonance frequency, or equivalently the spring constant of the harmonic oscillator, is set to zero, the Drude model (Eq. 4.11) is recovered.

For many metals, the optical properties are influenced by both free and bound electrons, where the bound electrons are described by multiple oscillators at varying frequencies and amplitudes. The DF can then be modeled by a combination of the Drude and Lorentz models, the Drude-Lorentz model

$$\varepsilon(\omega) = 1 - \frac{\omega_p^2}{\omega^2 + i\gamma\omega} + \sum_j \frac{\omega_{p,j}^2}{\omega_{0,j}^2 - \omega^2 - i\gamma\omega}, \tag{4.13}$$

where the sum is over all relevant Lorentz-type contributions (Fig. 4.1c). For such metals, the optical properties depend on where the bound electron contributions are spectrally localized with respect to the free electron behavior. This is, for example, the origin of the different colors of, e.g., gold and silver.

From the discussion in the Sect. 4.1, it is clear that the LSPR is intimately connected to the DF. In order for the resonance conditions Eq. 4.6 (spheres) and Eq. 4.6 (ellipsoids) to hold, however, the imaginary part of the DF has to be small or at least not highly varying. In Fig. 4.2, the dielectric functions for Pd, Au and Ag are shown. Ag and Au have qualitatively similar DFs with a sharp Drude-peak below 1 eV and an increase in the imaginary part at about 2 eV for Au and 4 eV for Ag which corresponds to the d-band onset, i.e., the distance between the d-band and the Fermi level [68]. The energy interval of the dip in the imaginary part of the DF below the d-band onset is ideal for strong LSPRs. The real part of the DF in this region corresponds to values at (Ag) or below (Ag and Au) the resonance condition (4.6), i.e. small spheres (Ag) or oblate ellipsoids (Au and Ag) should have strong LSPRs. For Pd, the imaginary part of the DF is very different since the d-band edge is positioned slightly above the Fermi level [68], which allows for transitions from the d-band at all energies. As a result, the imaginary part of the DF

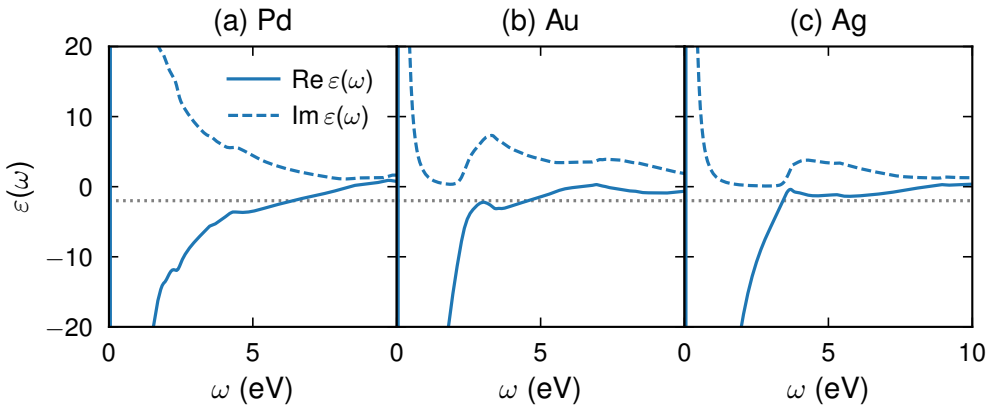

Figure 4.2: DFs for (a) Pd, (b) Au and (c) Ag obtained by *ab-initio* calculations from [68]. The grey line indicates $\mathrm{Re}\,\varepsilon(\omega) = -2$ which corresponds to the LSPR for small spheres according to Mie theory.

is large over a wide energy interval which causes significant damping of the LSPR. In addition, the resonance conditions from Mie theory do not necessarily hold and instead, the frequency of the LSPR will be the result of a trade-off between the real and imaginary contributions to the polarizability.

The bound electrons in the d-band can be viewed as multiple Lorentz-type oscillators that cause broad changes of the DF and general damping of the LSPR. In addition, metals can have spectrally localized interband transitions, corresponding to a single oscillator, which causes a pronounced feature in the DF similar to the schematic example in Fig. 4.1c [108, 109]. Such features cause an increase in absorption and scattering, similar to a LSPR. Contrary to a LSPR, however, an interband transition is a bulk phenomenon and as such does not depend on the geometry of the system. If an interband transition is spectrally close to a LSPR, they can couple which leads to avoided crossing behavior [108, 109]. In Paper II, we found that this phenomenon is crucial for understanding the size dependence of the optical response of hydrogenated Pd nanodisks as will be discussed in the following section.

4.3 Optical response of Pd–Au–H nanodisks

A qualitative understanding of the optical properties of the Pd–Au–H system in the Pd-rich end can be obtained from the DFs of pure Pd, $Pd_{75}Au_{25}$, and fully hydrogenated PdH (Fig. 4.3a-b). Addition of Au to Pd should, at some point, shift the d-band position below the Fermi level resulting in a decrease in the imaginary part of the DF as is characteristic for Au (Fig. 4.2b). The shift in the d-band position is, however, not linear [68] and up to 25% Au is not sufficient to significantly alter the DF short of a slight blue-shift of the real

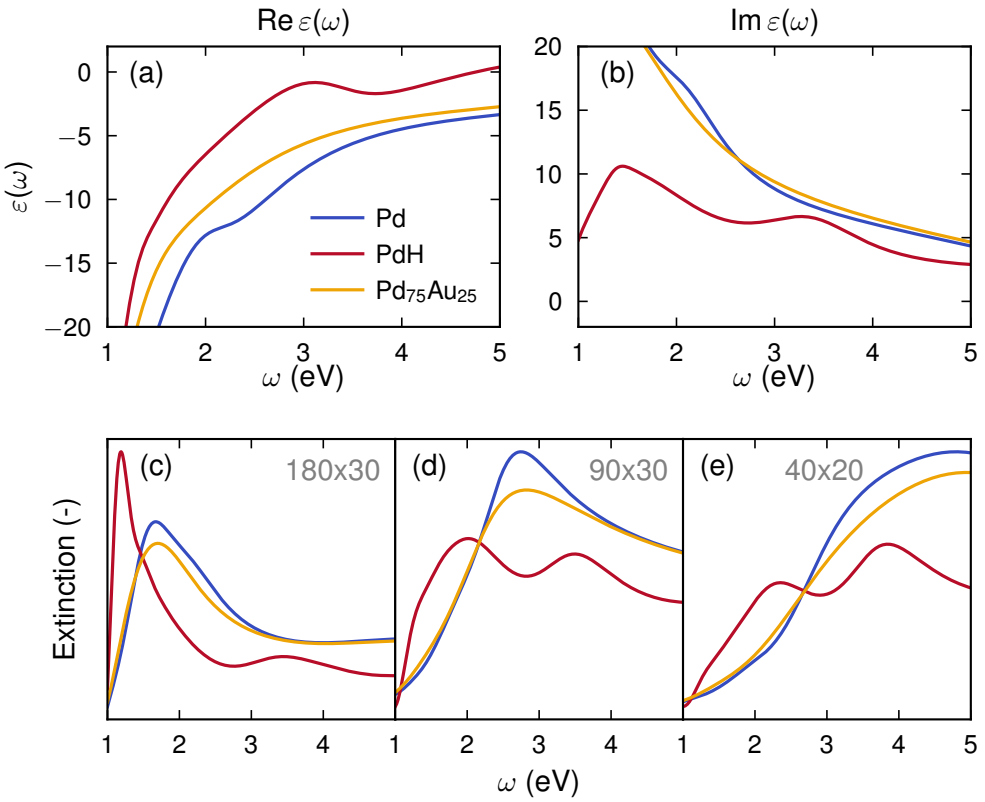

Figure 4.3: The (a) real and (b) imaginary part of the DF for Pd, PdH and $Pd_{75}Au_{25}$ calculated and fitted within the scope of Paper II and the corresponding extinction spectra for three nanodisk geometries calculated within the scope of Paper II (c-e). The size of the nanodisks are indicated by the grey labels as diameter × height in nm. Note that the extinction is normalized here, and generally the extinction increases with nanodisk volume.

part (Fig. 4.3a). The blue-shift of the real part could, according to Mie theory, result in a blue-shift of the LSPR. At the same time, the imaginary part increases with decreasing energy which make the predictions based on Mie theory ambiguous. In (Fig. 4.3c-e), the corresponding extinction spectra for three nanodisk geometries are shown. The difference between Pd and $Pd_{75}Au_{25}$ is small, and the introduction of Au seems to only lead to a slight broadening of the plasmon peak and no change in peak position. This effect could be explained by the combined effects of a blue-shift (caused by Re ε) and a broadening due to increased damping (caused by Im ε) where the latter would also cause a slight red-shift due to the asymmetry of the peak, resulting in negligible net shift of the peak position.

In Paper II, we show that the addition of H to Pd pushes the d-band edge to lower energies, crossing the Fermi level at about 50% H. As a result, the imaginary part of the

DF is significantly reduced for fully hydrogenated PdH (Fig. 4.3b). In addition, the real part of the DF display a significant blue-shift for PdH compared to Pd (Fig. 4.3a). These two factors indicates that the plasmon peak of PdH nanodisks should be blue-shifted in comparison to the case of Pd. Unlike the non-hydrogenated systems, the DF of PdH exhibit a distinct Lorentz-type feature at about 3.5 eV, which likely corresponds to an interband transition. The corresponding extinction spectra of the example nanodisks in Fig. 4.3c-e is significantly different for PdH compared to Pd. Most notably, the presumed interband transition gives rise to an additional peak at about 3.5 eV. This feature is more prominent for smaller nanodisks due to the fact that the amplitude of the LSPR increases with volume which reduces the relative amplitude of the interband transition-peak compared to the LSPR. In Paper II, we show that the two peaks exhibit avoided crossing behavior, which is characteristic for coupled LSPRs and interband transitions [108, 109]. Fig. 4.3c-e also shows the lower energy LSPR peak is blue-shifted compared to Pd as predicted. Lastly, the LSPR peak in Fig. 4.3c shows significant sharpening for the hydrogenated system, which is related to the dip in the imaginary part of the DF close to 1 eV.

5

Summary of papers

Paper I

Hydrogen-driven Surface Segregation in Pd-alloys from Atomic Scale Simulations

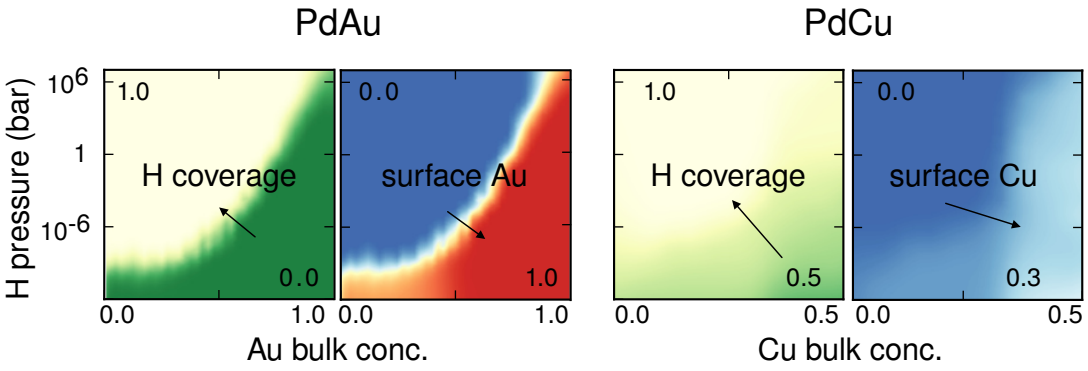

Figure 5.1: The H coverage and surface alloy composition as a function of bulk alloy composition and H_2 pressure for the Pd–Au and Pd–Cu systems.

The layer-by-layer surface segregation behavior of Pd–Au and Pd–Cu alloys is modeled as a function of H_2 pressure. fcc{111} surface slabs are modeled using CEs that are trained with DFT data and sampled in MC simulations. For the surface CEs, we introduce the concept of local symmetries (an effective merging of similar orbits) to reduce the number of parameters, which is found to increase the accuracy of the models. The effect of hydrogen is limited to adsorption at the surface, i.e., no absorption. This means

that the results are valid primarily in the pressure region before significant absorption occurs, as discussed in detail in the paper.

The resulting H surface coverage and alloy surface compositing are displayed in Fig. 5.1. For AuPd, we find that Au segregates to the surface in vacuum but as the H pressure is increased, the surface composition quickly switches to 100 % Pd, closely following the increase in H coverage from 0 to 100%. For CuPd, surface composition and H coverage vary gradually over a wide pressure interval and the behavior can be divided into three pressure regimes. At moderate to high H pressures ($\gtrsim 10^{-6}$ bar), the surface is covered with H and dominated by Pd. At lower pressures, the surface coverage decreases slightly and the surface composition increases in Cu. In complete vacuum (i.e., no H present, which corresponds to pressures below the range in Fig. 5.2), the surface is again depleted of Cu, which is coupled to a pronounced enrichment of Cu in the subsurface layer. This complex, non-monotonic behavior shines new light on an apparent discrepancy between primarily experimental and theoretical studies of surface segregation of the Pd–Cu system in vacuum.

Paper II

Computational Design of Alloy Nanostructures for Optical Sensing:
The Limits of Tuning Hydrogen Sensitivity via Composition and Geometry

The optical response of hydrogenated Pd-alloys is studied with the purpose of understanding the size and composition dependence of the hydrogen sensitivity in Pd-based nanodisks. First, the DFs are calculated for the Pd–Au–H system in the concentration range 0–33% Au and 0–100% H using time-dependent density-functional theory (TDDFT). Second, the extinction spectra for individual truncated-cone nanodisks on a silica substrate is calculated using FDTD simulations. The nanodisks cover a wide range of sizes with heights 20–40 nm and aspect ratios 2–12. Third, the hydrogen sensitivity, i.e., the ratio between the shift in optical response and H content, is analysed as a function of geometry and composition. The shift in optical response can be measured based on several different features. Here, we consider three different definitions based on extinction peak position, extinction amplitude at a certain wavelength, and wavelength onset of a particular extinction amplitude.

It is shown that the emergence of a second peak with increased H content is crucial for the H sensitivity. This is especially clear if the sensitivity is based on peak position (Fig. 5.2). Since the magnitude of the shift depends on which of the two peaks are dominating at high H content, which in turn depends on the disk size, a discontinuity is observed in the peak shift sensitivity as a function of disk diameter. For disk diameters above roughly 100 nm, the LSPR peak dominates and the sensitivity is approximately constant at 180 nm/c_H. Below 100 nm, however, the interband transition-peak domi-

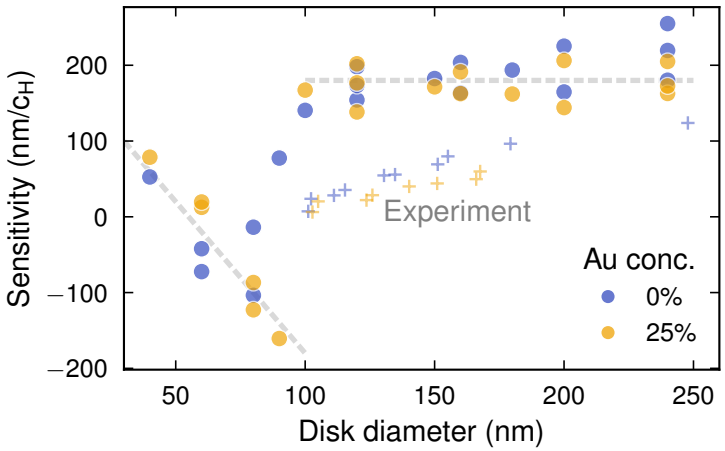

Figure 5.2: The hydrogen sensitivity in Pd–Au nanodisks based on the extinction peak shift vs. H uptake.

nates and sensitivity starts at a negative value and increases with decreased diameter, due to the relative shift in energy between the (constant) interband transition at high H content and the red-shifting LSPR at low H content. The corresponding experimental results from [15], for an array of disperse nanodisks, on the other hand, suggest a continuously increasing sensitivity. We believe the difference stems from broadening of the experimental optical response due to, e.g., size and grain boundary distribution and array effects, which effectively results in an averaging between particles with a negative and positive sensitivity. Although our results do not accurately predict the sensitivity of an array of disperse nanodisks, they suggest that there is an upper limit for the maximum sensitivity and that an increase in sensitivity can be achieved by producing more uniform nanodisks. In addition, they provide a physical explanation for the size dependence in the sensitivity.

6

Conclusions and outlook

In this thesis, thermodynamic and optical properties of Pd-nanoalloys in a hydrogen environment were studied using multiscale modeling. The aim was to answer two questions:

- What is the surface segregation behavior of Pd-alloys in different environments?
- How does the composition and geometry affect the optical response?

The segregation behavior has been successfully mapped out for Pd–Au and Pd–Cu alloys with varying H coverage for fcc-{111} surfaces. While these findings are enlightening for the H dependence specifically, further studies are needed in order to fully understand all aspects of surface segregation relevant for state-of-the-art experimental hydrogen sensors, in particular the effect of Cu on CO poisoning. This includes studies of the ternary Pd–Au–Cu system in contact with H, CO, and possibly other gases in multiple surface directions. In addition, in order to accurately describe the H interaction at high pressures, interstitial H sites should be included in the CE. This full system is significantly more complex to model as it consists of at least a three-component metal lattice (Pd/Au/Cu), a two-component interstitial lattice (H/vacancy) and a three-component surface lattice (H/CO/vacancy), i.e., 8 components compared to the 4 components in the present work. Still this can is in principle be achieved within the CE formalism.

A key advance made within this thesis is the introduction of local symmetries. This approach enables a modular view on CE construction where, for example, the bulk ECIs can be trained using a separate data set prior to training the remaining ECIs on the surface slab data. One could also imagine including ECIs for multiple surface orientations and eventually constructing a CE for a NP. This added flexibility is expected to facilitate CE construction especially as systems become more complex by, e.g., introducing interstitial H sites.

The optical response of single Pd-based nanodisks alloyed with a varying amount of Au has been simulated as a function of H uptake, resulting in an understanding of the composition and size dependence. Using the developed computational framework, an extension to additional geometries and alloyants would be straight-forward. A remaining challenge is to bridge the gap between the single particles studied within the scope of this thesis and the array of diverse nanodisks used in the proposed sensing platform.

6.1 Limitations

Modeling always comes with approximations and limitations. This is especially true in multiscale approaches where the accuracy of a modeling technique at a particular scale often imposes limits at another scale. For example, using a higher accuracy functional in the DFT calculations typically comes at an increased computational cost which might make the construction of CE models infeasible due to the large number of calculations required. Similarly, modeling the optical response of a random array of nanodisks would be difficult using FDTD simulations without decreasing the spatial and temporal resolution. The choices associated with each model are thus a compromise between accuracy at a certain level and providing enough information for the multiscale approach.

In the DFT calculations, the major source of approximation is the choice of functional. In this thesis, the vdW-DF-cx functional is chosen based on its good performance for similar systems compared to other functionals with similar computational cost. As discussed in Chapter 5, the vdW-DF-cx functional (as practically all other XC functionals) is, however, associated with an error in the surface energy calculations, which affects the credibility of the surface segregation predictions for Pd–Cu alloys. Other methods based on the random phase approximation (RPA) have shown better performance for surface and adsorption energies [110], at the price of a significant increase in computational cost. Another factor is the choice of wave function basis set. Here, plane waves are used which is the natural choice for periodic systems. The situation is, however, more complex since surface slabs (which change the boundary conditions) with adsorbates (which might benefit from localized orbitals) are studied. The plane waves are motivated based on the assumption that the separation between periodic images is large enough to avoid interaction and that the benefits for the crystalline metal system is greater than the possible disadvantages for the adsorbates.

Using CEs to model surface segregation in practice restricts the study to single crystalline, ideal surfaces. Real systems feature grain boundaries, multifaceted surfaces as well as surface defects, which might alter the surface segregation. The differences between the real and modeled systems are thus hard to disentangle since both the underlying *ab initio* method and/or the limitations of the CEs could be the cause. The lack of grain boundaries is also relevant for the optical properties since they are known to affect the hydrogenation process of hydrogen sensors [111].

Acknowledgments

First of all I wish to express my sincerest gratitude to my supervisor, Paul Erhart, for all of your support, encouragement, educational efforts, TV series recommendations and random youtube clips during the past three years. I would also like to thank my examiner, Henrik Grönbeck, for your guidance, and the Excellence Initiative Nano at Chalmers for providing a community and funding my research.

I would also like to thank all members of the CMM division for providing a fun and stimulating work environment where there is always time to help each other. I look forward to hopefully seeing more of you in person in the second half of my PhD studies.

Lastly, I would like to thank my friends and family for making my life outside of work a lot more fun. A special thanks to my husband, Olof, for being my favourite person and biggest supporter and to our (unborn) child for bringing me a lot of joy these past months (while not at all stealing all of my energy).

Bibliography

[1] S. Dutta, *A review on production, storage of hydrogen and its utilization as an energy resource,* Journal of Industrial and Engineering Chemistry **20**, 1148 (2014). doi:10.1016/j.jiec.2013.07.037.

[2] EG&G Technical Services, Inc., *Fuel cell handbook* (Morgantown, WV: U.S. Department of Energy, Office of Fossil Energy, National Energy Technology Laboratory, 2016). ISBN 978-1-365-10113-7.

[3] J. Kast, R. Vijayagopal, J. J. Gangloff, and J. Marcinkoski, *Clean commercial transportation: Medium and heavy duty fuel cell electric trucks,* International Journal of Hydrogen Energy **42**, 4508 (2017). doi:10.1016/j.ijhydene.2016.12.129.

[4] K. Kendall, M. Kendall, B. Liang, and Z. Liu, *Hydrogen vehicles in China: Replacing the Western Model,* International Journal of Hydrogen Energy **42**, 30179 (2017). doi:10.1016/j.ijhydene.2017.10.072.

[5] F. Zenith, R. Isaac, A. Hoffrichter, M. S. Thomassen, and S. Møller-Holst, *Techno-economic analysis of freight railway electrification by overhead line, hydrogen and batteries: Case studies in Norway and USA,* Proceedings of the Institution of Mechanical Engineers, Part F: Journal of Rail and Rapid Transit **234**, 791 (2020). doi:10.1177/0954409719867495.

[6] J. D. Holladay, J. Hu, D. L. King, and Y. Wang, *An overview of hydrogen production technologies,* Catalysis Today **139**, 244 (2009). doi:10.1016/j.cattod.2008.08.039.

[7] J. O. Abe, A. P. I. Popoola, E. Ajenifuja, and O. M. Popoola, *Hydrogen energy, economy and storage: Review and recommendation,* International Journal of Hydrogen Energy **44**, 15072 (2019). doi:10.1016/j.ijhydene.2019.04.068.

[8] Y. S. H. Najjar, *Hydrogen safety: The road toward green technology,* International Journal of Hydrogen Energy **38**, 10716 (2013). doi:10.1016/j.ijhydene.2013.05.126.

[9] X. Bévenot, A. Trouillet, C. Veillas, H. Gagnaire, and M. Clément, *Surface plasmon resonance hydrogen sensor using an optical fibre,* Measurement Science and Technology **13**, 118 (2001). doi:10.1088/0957-0233/13/1/315.

[10] P. Tobiška, O. Hugon, A. Trouillet, and H. Gagnaire, *An integrated optic hydrogen sensor based on SPR on palladium,* Sensors and Actuators B: Chemical **74**, 168 (2001). doi:10.1016/S0925-4005(00)00728-0.

[11] C. Langhammer, I. Zorić, B. Kasemo, and B. M. Clemens, *Hydrogen Storage in Pd Nanodisks Characterized with a Novel Nanoplasmonic Sensing Scheme,* Nano Letters **7**, 3122 (2007). doi:10.1021/nl071664a.

[12] C. Langhammer, E. M. Larsson, B. Kasemo, and I. Zorić, *Indirect Nanoplasmonic Sensing: Ultrasensitive Experimental Platform for Nanomaterials Science and Optical Nanocalorimetry,* Nano Letters **10**, 3529 (2010). doi:10.1021/nl101727b.

[13] N. Liu, M. L. Tang, M. Hentschel, H. Giessen, and A. P. Alivisatos, *Nanoantenna-Enhanced Gas Sensing in a Single Tailored Nanofocus,* Nat. Mater. **10**, 631 (2011). doi:10.1038/nmat3029.

[14] C. Boelsma, L. J. Bannenberg, M. J. van Setten, N.-J. Steinke, A. A. van Well, and B. Dam, *Hafnium — An Optical Hydrogen Sensor Spanning Six Orders in Pressure,* Nat. Commun. **8**, 15718 (2017). doi:10.1038/ncomms15718.

[15] F. A. A. Nugroho, I. Darmadi, V. P. Zhdanov, and C. Langhammer, *Universal Scaling and Design Rules of Hydrogen-Induced Optical Properties in Pd and Pd-Alloy Nanoparticles,* ACS Nano **12**, 9903 (2018). doi:10.1021/acsnano.8b02835.

[16] X. She, Y. Shen, J. Wang, and C. Jin, *Pd Films on Soft Substrates: A Visual, High-Contrast and Low-Cost Optical Hydrogen Sensor,* Light Sci. Appl. **8**, 4 (2019). https://www.nature.com/articles/s41377-018-0114-x.

[17] T. Beni, N. Yamasaku, T. Kurotsu, N. To, S. Okazaki, T. Arakawa, A. Balčytis, G. Seniutinas, S. Juodkazis, and Y. Nishijima, *Metamaterial for Hydrogen Sensing,* ACS Sens. **4**, 2389 (2019). doi:10.1021/acssensors.9b00980.

[18] F. A. A. Nugroho, I. Darmadi, L. Cusinato, A. Susarrey-Arce, H. Schreuders, L. J. Bannenberg, A. Bastos da Silva Fanta, S. Kadkhodazadeh, J. B. Wagner, T. J. Antosiewicz, A. Hellman, V. P. Zhdanov, B. Dam, and C. Langhammer, *Metal–Polymer Hybrid Nanomaterials for Plasmonic Ultrafast Hydrogen Detection,* Nat. Mater. **18**, 489 (2019). doi:10.1038/s41563-019-0325-4.

[19] F. Sterl, N. Strohfeldt, S. Both, E. Herkert, T. Weiss, and H. Giessen, *Design Principles for Sensitivity Optimization in Plasmonic Hydrogen Sensors,* ACS Sens. **5**, 917 (2020). doi:10.1021/acssensors.9b02436.

[20] L. Bannenberg, H. Schreuders, and B. Dam, *Tantalum-Palladium: Hysteresis-Free Optical Hydrogen Sensor Over 7 Orders of Magnitude in Pressure with Sub-Second Response,* Adv. Funct. Mater. **31**, 2010483 (2021). doi:10.1002/adfm.202010483.

[21] M. Losurdo, Y. Gutiérrez, A. Suvorova, M. M. Giangregorio, S. Rubanov, A. S. Brown, and F. Moreno, *Gallium Plasmonic Nanoantennas Unveiling Multiple Kinetics of Hydrogen Sensing, Storage, and Spillover,* Adv. Mater. **33**, 2100500 (2021). doi:10.1002/adma.202100500.

[22] K. Hassan, A. S. M. Iftekhar Uddin, and G.-S. Chung, *Fast-Response Hydrogen Sensors Based on Discrete Pt/Pd Bimetallic Ultra-Thin Films,* Sens. Actuators, B **234**, 435 (2016). doi:10.1016/j.snb.2016.05.013.

[23] S. Kabcum, D. Channei, A. Tuantranont, A. Wisitsoraat, C. Liewhiran, and S. Phanichphant, *Ultra-Responsive Hydrogen Gas Sensors Based on PdO Nanoparticle-Decorated WO_3 Nanorods Synthesized by Precipitation and Impregnation Methods,* Sens. Actuators, B **226**, 76 (2016). doi:10.1016/j.snb.2015.11.120.

[24] E. K. Alenezy, Y. M. Sabri, A. E. Kandjani, D. Korcoban, S. S. A. Abdul Haroon Rashid, S. J. Ippolito, and S. K. Bhargava, *Low-Temperature Hydrogen Sensor: Enhanced Performance*

Enabled through Photoactive Pd-Decorated TiO_2 Colloidal Crystals, ACS Sens. **5**, 3902 (2020). doi:10.1021/acssensors.0c01387.

[25] M. L. Tang, N. Liu, J. A. Dionne, and A. P. Alivisatos, *Observations of Shape-Dependent Hydrogen Uptake Trajectories from Single Nanocrystals,* Journal of the American Chemical Society **133**, 13220 (2011). doi:10.1021/ja203215b.

[26] M. A. Poyli, V. M. Silkin, I. P. Chernov, P. M. Echenique, R. D. Muiño, and J. Aizpurua, *Multiscale Theoretical Modeling of Plasmonic Sensing of Hydrogen Uptake in Palladium Nanodisks,* J. Phys. Chem. Lett. **3**, 2556 (2012). doi:10.1021/jz3007723.

[27] C. Wadell, F. A. A. Nugroho, E. Lidström, B. Iandolo, J. B. Wagner, and C. Langhammer, *Hysteresis-Free Nanoplasmonic Pd-Au Alloy Hydrogen Sensors,* Nano Letters **15**, 3563 (2015). doi:10.1021/acs.nanolett.5b01053.

[28] A. Maeland and T. B. Flanagan, *X-Ray and Thermodynamic Studies of the Absorption of Hydrogen by Gold-Palladium Alloys,* The Journal of Physical Chemistry **69**, 3575 (1965). doi:10.1021/j100894a054.

[29] I. Darmadi, F. A. A. Nugroho, S. Kadkhodazadeh, J. B. Wagner, and C. Langhammer, *Rationally Designed PdAuCu Ternary Alloy Nanoparticles for Intrinsically Deactivation-Resistant Ultrafast Plasmonic Hydrogen Sensing,* ACS Sensors **4**, 1424 (2019). doi:10.1021/acssensors.9b00610.

[30] I. Darmadi, S. Z. Khairunnisa, D. Tomeček, and C. Langhammer, *Optimization of the Composition of PdAuCu Ternary Alloy Nanoparticles for Plasmonic Hydrogen Sensing,* ACS Applied Nano Materials **4**, 8716 (2021). doi:10.1021/acsanm.1c01242.

[31] G. Kresse and J. Hafner, *Ab initio molecular dynamics for liquid metals,* Physical Review B **47**, 558 (1993). doi:10.1103/PhysRevB.47.558.

[32] G. Kresse and J. Furthmüller, *Efficiency of ab-initio total energy calculations for metals and semiconductors using a plane-wave basis set,* Computational Materials Science **6**, 15 (1996). doi:10.1016/0927-0256(96)00008-0.

[33] R. M. Martin, *Electronic Structure : Basic Theory and Practical Methods* (Cambridge : Cambridge Univ. Press, 2004., 2004). ISBN 978-0-521-78285-2.

[34] M. Born and R. Oppenheimer, *Zur Quantentheorie der Molekeln,* Annalen der Physik **389**, 457 (1927). doi:10.1002/andp.19273892002.

[35] P. Hohenberg and W. Kohn, *Inhomogeneous Electron Gas,* Physical Review **136**, B864 (1964). doi:10.1103/PhysRev.136.B864.

[36] W. Kohn and L. J. Sham, *Self-Consistent Equations Including Exchange and Correlation Effects,* Physical Review **140**, A1133 (1965). doi:10.1103/PhysRev.140.A1133.

[37] P. E. Blöchl, *Projector augmented-wave method,* Physical Review B **50**, 17953 (1994). doi:10.1103/PhysRevB.50.17953.

[38] G. Kresse and D. Joubert, *From ultrasoft pseudopotentials to the projector augmented-wave method,* Physical Review B **59**, 1758 (1999). doi:10.1103/PhysRevB.59.1758.

[39] E. S. Sachs, J. Hinze, and N. H. Sabelli, *Frozen core approximation, a pseudopotential method tested on six states of NaH,* The Journal of Chemical Physics **62**, 3393 (1975). doi:10.1063/1.430993.

[40] J. P. Perdew and Y. Wang, *Accurate and simple analytic representation of the electron-gas correlation energy,* Physical Review B **45**, 13244 (1992). doi:10.1103/PhysRevB.45.13244.

[41] J. P. Perdew, K. Burke, and M. Ernzerhof, *Generalized Gradient Approximation Made Simple,* Physical Review Letters **77**, 3865 (1996). doi:10.1103/PhysRevLett.77.3865.

[42] J. P. Perdew, A. Ruzsinszky, G. I. Csonka, O. A. Vydrov, G. E. Scuseria, L. A. Constantin, X. Zhou, and K. Burke, *Restoring the Density-Gradient Expansion for Exchange in Solids and Surfaces,* Physical Review Letters **100**, 136406 (2008). doi:10.1103/PhysRevLett.100.136406.

[43] M. Dion, H. Rydberg, E. Schröder, D. C. Langreth, and B. I. Lundqvist, *Van der Waals Density Functional for General Geometries,* Physical Review Letters **92**, 246401 (2004). doi:10.1103/PhysRevLett.92.246401.

[44] K. Lee, É. D. Murray, L. Kong, B. I. Lundqvist, and D. C. Langreth, *Higher-accuracy van der Waals density functional,* Physical Review B **82**, 081101 (2010). doi:10.1103/PhysRevB.82.081101.

[45] K. Berland and P. Hyldgaard, *Exchange functional that tests the robustness of the plasmon description of the van der Waals density functional,* Physical Review B **89**, 035412 (2014). doi:10.1103/PhysRevB.89.035412.

[46] K. Berland, V. R. Cooper, K. Lee, E. Schröder, T. Thonhauser, P. Hyldgaard, and B. I. Lundqvist, *van der Waals forces in density functional theory: a review of the vdW-DF method,* Reports on Progress in Physics **78**, 066501 (2015). doi:10.1088/0034-4885/78/6/066501.

[47] J. Löfgren, *Modeling colloidal nanoparticles: From growth to deposition*. PhD thesis, Chalmers University of Technology, Gothenburg, 2019.

[48] L. Gharaee, P. Erhart, and P. Hyldgaard, *Finite-temperature properties of nonmagnetic transition metals: Comparison of the performance of constraint-based semilocal and nonlocal functionals,* Physical Review B **95**, 085147 (2017). doi:10.1103/PhysRevB.95.085147.

[49] J. Löfgren, J. M. Rahm, J. Brorsson, and P. Erhart, *Computational assessment of the efficacy of halides as shape-directing agents in nanoparticle growth,* Physical Review Materials **4**, 096001 (2020). doi:10.1103/PhysRevMaterials.4.096001.

[50] J. M. Sanchez, F. Ducastelle, and D. Gratias, *Generalized Cluster Description of Multicomponent Systems,* Physica A: Statistical Mechanics and its Applications **128**, 334 (1984). doi:10.1016/0378-4371(84)90096-7.

[51] M. Ångqvist, W. A. Muñoz, J. M. Rahm, E. Fransson, C. Durniak, P. Rozyczko, T. H. Rod, and P. Erhart, *ICET – A Python Library for Constructing and Sampling Alloy Cluster Expansions,* Advanced Theory and Simulations **0**, 1900015 (2019). doi:10.1002/adts.201900015.

[52] A. van de Walle, *Multicomponent Multisublattice Alloys, Nonconfigurational Entropy and Other Additions to the Alloy Theoretic Automated Toolkit,* Calphad **33**, 266 (2009). doi:10.1016/j.calphad.2008.12.005.

[53] R. Tibshirani, *Regression Shrinkage and Selection Via the Lasso,* Journal of the Royal Statistical Society: Series B (Methodological) **58**, 267 (1996). doi:10.1111/j.2517-6161.1996.tb02080.x.

[54] D. J. C. MacKay, *Bayesian Non-linear Modelling for the Prediction Competition,* ASHRAE Transactions, V.100, Pt.2 , 1053 (1994).

[55] A. Walle and G. Ceder, *Automating first-principles phase diagram calculations,* Journal of Phase Equilibria **23**, 348 (2002). doi:10.1361/105497102770331596.

[56] G. L. W. Hart and R. W. Forcade, *Algorithm for Generating Derivative Structures,* Physical Review B **77**, 224115 (2008). doi:10.1103/PhysRevB.77.224115.

[57] G. L. W. Hart and R. W. Forcade, *Generating Derivative Structures from Multilattices: Algorithm and Application to Hcp Alloys,* Physical Review B **80**, 014120 (2009). doi:10.1103/PhysRevB.80.014120.

[58] D. Lerch, O. Wieckhorst, G. L. W. Hart, R. W. Forcade, and S. Müller, *UNCLE: a code for constructing cluster expansions for arbitrary lattices with minimal user-input,* Modelling and Simulation in Materials Science and Engineering **17**, 055003 (2009). doi:10.1088/0965-0393/17/5/055003.

[59] A. Seko, Y. Koyama, and I. Tanaka, *Cluster expansion method for multicomponent systems based on optimal selection of structures for density-functional theory calculations,* Physical Review B **80**, 165122 (2009). doi:10.1103/PhysRevB.80.165122.

[60] L. J. Nelson, V. Ozoliņš, C. S. Reese, F. Zhou, and G. L. W. Hart, *Cluster expansion made easy with Bayesian compressive sensing,* Physical Review B **88**, 155105 (2013). doi:10.1103/PhysRevB.88.155105.

[61] J. H. Chang, D. Kleiven, M. Melander, J. Akola, J. M. Garcia-Lastra, and T. Vegge, *CLEASE: a versatile and user-friendly implementation of cluster expansion method,* Journal of Physics: Condensed Matter **31**, 325901 (2019). doi:10.1088/1361-648X/ab1bbc.

[62] D. Kleiven, J. Akola, A. A. Peterson, T. Vegge, and J. H. Chang, *Training sets based on uncertainty estimates in the cluster-expansion method,* Journal of Physics: Energy **3**, 034012 (2021). doi:10.1088/2515-7655/abf9ef.

[63] J. M. Thijssen, *Computational Physics* (Cambridge : Cambridge University Press, 2007., 2007). ISBN 978-0-521-83346-2.

[64] N. Metropolis, A. W. Rosenbluth, M. N. Rosenbluth, A. H. Teller, and E. Teller, *Equation of State Calculations by Fast Computing Machines,* The Journal of Chemical Physics **21**, 1087 (1953). doi:10.1063/1.1699114.

[65] D. A. Kofke and E. D. Glandt, *Nearly monodisperse fluids. I. Monte Carlo simulations of Lennard-Jones particles in a semigrand ensemble,* The Journal of Chemical Physics **87**, 4881 (1987). doi:10.1063/1.452800.

[66] S. Kirkpatrick, C. D. Gelatt, and M. P. Vecchi, *Optimization by Simulated Annealing,* Science **220**, 671 (1983). doi:10.1126/science.220.4598.671.

[67] A. Taflove and S. C. Hagness, *Computational electrodynamics : the finite-difference time-domain method* (Boston: Artech House, 2005). ISBN 1-58053-832-0.

[68] J. M. Rahm, C. Tiburski, T. P. Rossi, F. A. A. Nugroho, S. Nilsson, C. Langhammer, and P. Erhart, *A Library of Late Transition Metal Alloy Dielectric Functions for Nanophotonic Applications,* Advanced Functional Materials **30**, 2002122 (2020). doi:10.1002/adfm.202002122.

[69] A. F. Oskooi, D. Roundy, M. Ibanescu, P. Bermel, J. Joannopoulos, and S. G. Johnson, *Meep: A flexible free-software package for electromagnetic simulations by the FDTD method,* Computer Physics Communications **181**, 687 (2010). doi:10.1016/j.cpc.2009.11.008.

[70] K. Yee, *Numerical solution of initial boundary value problems involving maxwell's equations in isotropic media,* IEEE Transactions on Antennas and Propagation **14**, 302 (1966). doi:10.1109/TAP.1966.1138693.

[71] R. Lässer and K. H. Klatt, *Solubility of hydrogen isotopes in palladium,* Physical Review B **28**, 748 (1983). doi:10.1103/PhysRevB.28.748.

[72] D. Schroeder, *An introduction to thermal physics* (San Francisco, CA: Addison Wesley, 2000). ISBN 0-201-38027-7.

[73] E. Wicke and J. Blaurock, *New experiments on and interpretations of hysteresis effects of Pd-D2 and Pd-H2,* Journal of the Less Common Metals **130**, 351 (1987). doi:10.1016/0022-5088(87)90129-9.

[74] P. Subramanian and D. Laughlin, *Cu-Pd (Copper-Palladium),* Journal of Phase Equilibria **12**, 231 (1991). doi:10.1007/BF02645723.

[75] Y. Fukai, *The metal-hydrogen system : basic bulk properties* (Berlin New York: Springer, 2005). ISBN 978-3-540-28883-1.

[76] H. Okamoto and T. B. Massalski, *The Au–Pd (Gold-Palladium) system,* Bulletin of Alloy Phase Diagrams **6**, 229 (1985). doi:10.1007/BF02880404.

[77] S. Luo, D. Wang, and T. B. Flanagan, *Thermodynamics of Hydrogen in fcc Pd–Au Alloys,* The Journal of Physical Chemistry B **114**, 6117 (2010). doi:10.1021/jp100858r.

[78] Y. Sakamoto, N. Ishimaru, and Y. Mukai, *Thermodynamics of Solution of Hydrogen in Pd-Cu and Pd-Cu-Au Solid Solution Alloys,* Berichte der Bunsengesellschaft für physikalische Chemie **95**, 680 (1991). doi:10.1002/bbpc.19910950605.

[79] G. Wulff, *XXV. Zur Frage der Geschwindigkeit des Wachsthums und der Auflösung der Krystallflächen,* Zeitschrift für Kristallographie - Crystalline Materials **34**, 449 (1901). doi:10.1524/zkri.1901.34.1.449.

[80] W. R. Tyson and W. A. Miller, *Surface free energies of solid metals: Estimation from liquid surface tension measurements,* Surface Science **62**, 267 (1977). doi:10.1016/0039-6028(77)90442-3.

[81] A. R. Miedema, *Surface Segregation in Alloys of Transition Metals,* International Journal of Materials Research **69**, 455 (1978). doi:10.1515/ijmr-1978-690706.

[82] F. F. Abraham, *Surface Segregation in Binary Solid Solutions: The $\gamma^* - \sigma^*$ Representation,* Physical Review Letters **46**, 546 (1981). doi:10.1103/PhysRevLett.46.546.

[83] J. R. Chelikowsky, *Predictions for surface segregation in intermetallic alloys,* Surface Science **139**, L197 (1984). doi:10.1016/0039-6028(84)90047-5.

[84] D. Tománek, A. A. Aligia, and C. A. Balseiro, *Calculation of elastic strain and electronic effects on surface segregation,* Physical Review B **32**, 5051 (1985). doi:10.1103/PhysRevB.32.5051.

[85] F. Ducastelle, B. Legrand, and G. Tréglia, *Surface Segregation in Transition Metal Alloys: From Electronic Structure to Phase Portraits,* Progress of Theoretical Physics Supplement **101**, 159 (1990). doi:10.1143/PTP.101.159.

[86] D. Tománek, S. Mukherjee, V. Kumar, and K. H. Bennemann, *Calculation of chemisorption and absorption induced surface segregation,* Surface Science **114**, 11 (1982). doi:10.1016/0039-6028(82)90452-6.

[87] G. Bozzolo, J. E. Garcés, R. D. Noebe, P. Abel, and H. O. Mosca, *Atomistic modeling of surface and bulk properties of Cu, Pd and the Cu-Pd system,* Progress in Surface Science **73**, 79 (2003). doi:10.1016/j.progsurf.2003.08.034.

[88] O. M. Løvvik, *Surface segregation in palladium based alloys from density-functional calculations,* Surface Science **583**, 100 (2005). doi:10.1016/j.susc.2005.03.028.

[89] I. Atanasov and M. Hou, *Equilibrium ordering properties of Au-Pd alloys and nanoalloys,* Surface Science **603**, 2639 (2009). doi:10.1016/j.susc.2009.06.018.

[90] F. Calvo, *Thermodynamics of nanoalloys,* Physical Chemistry Chemical Physics **17**, 27922 (2015). doi:10.1039/C5CP00274E.

[91] J. R. Boes and J. R. Kitchin, *Modeling Segregation on AuPd(111) Surfaces with Density Functional Theory and Monte Carlo Simulations,* The Journal of Physical Chemistry C **121**, 3479 (2017). doi:10.1021/acs.jpcc.6b12752.

[92] M. Zhao, W. G. Sloof, and A. Bottger, *Modelling of surface segregation for palladium alloys in vacuum and gas environments,* International Journal of Hydrogen Energy **43**, 2212 (2018). doi:10.1016/j.ijhydene.2017.12.039.

[93] M. Mamatkulov, I. V. Yudanov, A. V. Bukhtiyarov, and K. M. Neyman, *Pd Single-Atom Sites on the Surface of PdAu Nanoparticles: A DFT-Based Topological Search for Suitable Compositions,* Nanomaterials **11**, 122 (2021). doi:10.3390/nano11010122.

[94] Z.-J. Wang, J. Chen, Y. Huang, and Z.-X. Chen, *Surface segregation of PdM (M=Cu, Ag, Au) alloys and its implication to acetylene hydrogenation, DFT-based Monte Carlo simulations,* Materials Today Communications **28**, 102475 (2021). doi:10.1016/j.mtcomm.2021.102475.

[95] Y. Yang, Z. Guo, A. J. Gellman, and J. R. Kitchin, *Simulating Segregation in a Ternary Cu–Pd–Au Alloy with Density Functional Theory, Machine Learning, and Monte Carlo Simulations,* The Journal of Physical Chemistry C **126**, 1800 (2022). doi:10.1021/acs.jpcc.1c09647.

[96] S. K. Gade, E. A. Payzant, H. J. Park, P. M. Thoen, and J. D. Way, *The effects of fabrication and annealing on the structure and hydrogen permeation of Pd–Au binary alloy membranes,* Journal of Membrane Science **340**, 227 (2009). doi:10.1016/j.memsci.2009.05.034.

[97] M. Okube, V. Petrykin, J. E. Mueller, D. Fantauzzi, P. Krtil, and T. Jacob, *Topologically Sensitive Surface Segregations of Au–Pd Alloys in Electrocatalytic Hydrogen Evolution,* ChemElectroChem **1**, 207 (2014). doi:10.1002/celc.201300112.

[98] J. B. Miller, C. Matranga, and A. J. Gellman, *Surface segregation in a polycrystalline Pd70Cu30 alloy hydrogen purification membrane,* Surface Science **602**, 375 (2008). doi:10.1016/j.susc.2007.10.031.

[99] D. Priyadarshini, P. Kondratyuk, Y. N. Picard, B. D. Morreale, A. J. Gellman, and J. B. Miller, *High-Throughput Characterization of Surface Segregation in Cu_xPd_{1-x} Alloys,* The Journal of Physical Chemistry C **115**, 10155 (2011). doi:10.1021/jp201793d.

[100] C. Yin, Z. Guo, and A. J. Gellman, *Surface Segregation Across Ternary Alloy Composition Space: $Cu_x Au_y Pd_{1-x-y}$,* The Journal of Physical Chemistry C , acs.jpcc.0c02058 (2020). doi:10.1021/acs.jpcc.0c02058.

[101] F. Cheng, X. He, Z.-X. Chen, and Y.-G. Huang, *Kinetic Monte Carlo simulation of surface segregation in Pd-Cu alloys,* Journal of Alloys and Compounds **648**, 1090 (2015). doi:10.1016/j.jallcom.2015.05.286.

[102] L. Yang, *Reverse surface segregation in Cu-Pd bimetallic catalysts at low concentrations of Cu,* Philosophical Magazine A **80**, 1879 (2000). doi:10.1080/01418610008219091.

[103] L. Pielsticker, I. Zegkinoglou, Z.-K. Han, J. J. Navarro, S. Kunze, O. Karslıoğlu, S. V. Levchenko, and B. Roldan Cuenya, *Crystallographic Orientation Dependence of Surface Segregation and Alloying on PdCu Catalysts for CO_2 Hydrogenation,* The Journal of Physical Chemistry Letters **12**, 2570 (2021). doi:10.1021/acs.jpclett.1c00179.

[104] J. L. Rousset, J. C. Bertolini, and P. Miegge, *Theory of segregation using the equivalent-medium approximation and bond-strength modifications at surfaces: Application to fcc Pd-X alloys,* Physical Review B **53**, 4947 (1996). doi:10.1103/PhysRevB.53.4947.

[105] X. Zhang, W. Wang, J. Liu, S. Sheng, G. Xiong, and W. Yang, *Hydrogen transport through thin palladium-copper alloy composite membranes at low temperatures,* Thin Solid Films **516**, 1849 (2008). doi:10.1016/j.tsf.2007.08.132.

[106] Z.-K. Han, D. Sarker, M. Troppenz, S. Rigamonti, C. Draxl, W. A. Saidi, and S. V. Levchenko, *First-principles study of Pd-alloyed Cu(111) surface in hydrogen atmosphere at realistic temperatures,* Journal of Applied Physics **128**, 145302 (2020). doi:10.1063/5.0020625.

[107] C. Bohren and D. R. Huffman, *Absorption and scattering of light by small particles* (New York: Wiley, 1983). ISBN 0-471-29340-7.

[108] T. Pakizeh, *Optical Absorption of Plasmonic Nanoparticles in Presence of a Local Interband Transition,* J. Phys. Chem. C **115**, 21826 (2011). doi:10.1021/jp207413h.

[109] Z. Pirzadeh, T. Pakizeh, V. Miljkovic, C. Langhammer, and A. Dmitriev, *Plasmon–Interband Coupling in Nickel Nanoantennas,* ACS Photonics **1**, 158 (2014). doi:10.1021/ph4000339.

[110] L. Schimka, J. Harl, A. Stroppa, A. Grüneis, M. Marsman, F. Mittendorfer, and G. Kresse, *Accurate surface and adsorption energies from many-body perturbation theory,* Nature Materials **9**, 741 (2010). doi:10.1038/nmat2806.

[111] S. Alekseeva, A. B. d. S. Fanta, B. Iandolo, T. J. Antosiewicz, F. A. A. Nugroho, J. B. Wagner, A. Burrows, V. P. Zhdanov, and C. Langhammer, *Grain boundary mediated hydriding phase transformations in individual polycrystalline metal nanoparticles,* Nature Communications **8**, 1084 (2017). doi:10.1038/s41467-017-00879-9.